ADVANCED STEREOSCOPY TOWARDS ON-MACHINE SURFACE METROLOGY AND INSPECTION

A Dissertation

by

XIANGYU GUO

Submitted to the Graduate and Professional School of
Texas A&M University
in partial fulfillment of the requirements for the degree of

DOCTOR OF PHILOSOPHY

Chair of Committee,	ChaBum Lee
Committee Members,	Bruce Tai
	Waruna Kulatilaka
	Felipe Guzmán
Head of Department,	Guillermo Aguilar

May 2022

Major Subject: Mechanical Engineering

ABSTRACT

With the goal of inventing an integral on-machine integral 3D machine vision inspection system, which monitors the parts quality and extract required patterns or structures during the manufacturing process using low-cost hardware and in a high-speed mode, this dissertation discussed the newly developed strobe-stereoscopy (SS) technique for in- motion targets examination. Stereoscopy is utilized for 3D reconstruction from recorded image pairs based on the triangulation of the display pixels, test target, and cameras. Stroboscopy is introduced to lock the moving target at different locations by frequency matching between the light source and the controlled motor.

Fluorescent fluid was introduced and implemented to the SS system for high-gloss reflective surface inspection. Stereoscopy technique is limited on the diffused surface because of the sensitivity to illumination dispersion, fluorescent strobe-stereoscopy (FSS) technique overcomes the limitation to polished surface inspection and is applied to step- by-step fabrication process monitoring thus complete the metrology-in-loop for the automated production. The surface filtering-based image selection and extraction approach (ISE) is created for quick pattern extraction from the freeform base structure, which was integrated into the built hardware configuration.

In this dissertation, the performance of inspection systems has been analyzed and validated with comprehensive experiment results. Potential and future work of the proposed technique was included as well.

DEDICATION

To my parents, Yingfu Guo and Haiyan Liu.

ACKNOWLEDGEMENTS

I would like to thank my dissertation advisor, Dr. ChaBum Lee, for providing me with the exciting opportunities to work on machine vision surface inspection projects. It has been an honor to work on so many challenging projects. Thanks to my committee members, Dr. Tai, Dr. Kulatilaka, and Dr. Guzmán, for their guidance and support throughout this research.

Thanks to all the lab mates and other group members for all the discussions on the projects, researches, and working together to solve the problems. I am proud to be a member of this great group!

Thanks also to my parents, Yingfu Guo and Haiyan Liu, for providing me with continuous encouragement and reminding me never to give up. Thanks to my boyfriend, Thomas Achee, for your constant companion along the journey. And to Jonathan, thanks for reminding me to look at the beautiful heavens above.

CONTRIBUTORS AND FUNDING SOURCES

Contributors

This work was supervised by a dissertation committee consisting of Dr. ChaBum Lee, Dr. Bruce Tai, and Dr. Waruna Kulatilaka of the Department of Mechanical Engineering and Dr. Felipe Guzmán of the Department of Aerospace Engineering.

The reference target data analyzed for validation the capability of proposed system was provided by Honeywell Manufacturing Technologies LLC (DOE-contracted), and measured by Zeiss CMM. All other work conducted for the dissertation was completed by the student independently.

NOMENCLATURE

SS	Strobo-Stereoscopy
FSS	Fluorescent Strobo-Stereocopy
ISE	Image Segmentation and Extraction
FOV	Field of View
FFOV	Full Field of View
LDS	Laser Displacement Sensor

TABLE OF CONTENTS

Page

ABSTRACT ii

DEDICATION iii

ACKNOWLEDGEMENTS iv

CONTRIBUTORS AND FUNDING SOURCES v

NOMENCLATURE vi

TABLE OF CONTENTS vii

LIST OF FIGURES ix

LIST OF TABLES xiii

1. INTRODUCTION 1

    1.1. Current Surface Quality Inspection System 1
        1.1.1. Metrology requirements for automated mass production 2
        1.1.2. Surface quality inspection techniques 4
    1.2. Motivation 9
    1.3. Dissertation Overview 11

2. STEREOSCOPY METROLOGY OVERVIEW 13

    2.1. History of Stereoscopy 13
    2.2. Stereoscopy Principle 14
    2.3. Stereoscopy System Applications, Design criteria and Challenges 20

3. STROBO-STEREOSCOPY* 23

    3.1. Stroboscopy Effect 23
    3.2. Strobo-Stereoscopy Methodology 24
    3.3. Synchronizing the Flash of Stroboscopic Light with the Motion of the Rotating Objects 25
    3.4. 3D Surface Reconstruction 28
    3.5. Experiment and Results 31

3.5.1. Experiment setup 31
3.5.2. Phase-locked mode 32
3.5.3. Phase shifting mode 34
3.5.4. Rough surface target measurement 35
3.6. Conclusion 38

4. FLUORESCENT STROBO-STEREOSCOPY* 40

4.1. Fluorescent Fluid 40
4.2. Fluid Intermedia Effect 42
4.3. Fluorescent Strobo-Stereoscopy Methodology 43
4.4. Experiment Results 47
4.4.1. Surface quality effects under FSS methods comparison 48
4.4.2. FSS on patterned surface 51
4.4.3. Dimensional errors inspection 55
4.5. Conclusion 57

5. IMAGE SEGMENTATION AND EXTRACTION POST-PROCESSING TECHNIQUE* 59

5.1. Image Segmentation Techniques Overview 59
5.1.1. 3D imaging process applied fields 59
5.1.2. Requirements for implemented 3D image processing 61
5.2. Image Segmentation and Extraction Principle 62
5.3. Experiments and Results 66
5.3.1. Stereoscopy based on ISE method 66
5.3.2. Strobo-Stereoscopy based ISE method 71
5.4. Conclusion 76

6. SUMMARY 77

6.1. Conclusion 77
6.2. Limitation and Future work 78

REFERENCES 83

APPENDIX A CV 96

LIST OF FIGURES

Page

Figure 1.1 Applications distribution for process control during the manufacturing based on the Depth of field/Object size and Depth uncertainty. 3

Figure 1.2 Applications distribution for common surface metrology techniques based on the Depth of field/Object size and Depth uncertainty. 5

Figure 1.3 Research motivation, objectives and proposed solution. 10

Figure 2.1. Stereoscopic system principle 14

Figure 2.2. Effect of lens distortion. (a) and (b) show the effect of p_1 and p_2 , where p_2 = 0 in (a) and p_1 =0 in(b).(c)and(d)show the effect of $q_1$and q_2 ,where q_2 =0in(c)and q_1 =0 in(d). 18

Figure 2.3. Effect of camera radial distortion $k1$, (a) $k1$ is positive (b) $k1$ is negative. 19

Figure 3.1 Strobo-stereoscopy methodology. 24

Figure 3.2 Flow chart of stroboscopic motion and light control algorithms. i is a positive integer. 26

Figure 3.3 Whole view 3D surface building process 27

Figure 3.4. 3D Printed reference array. 28

Figure 3.5. Stereoscopic reconstruction process (a), example on stereoscopic reconstruction process (b), depth map(c) and system error removed and filtered map (d). 29

Figure 3.6. 3D printed part surface map (a), the linear extract measurement in the blue arrow line location (b), dial-gauge measured height variation (c), and dial-gauge measurement set-up (d). 30

Figure 3.7. Experiment set-up of the proposed method (a) and experiment target end mill tool sample (b). 31

Figure 3.8. End mill tool phase-locked surface map at 90 RPM (a) and 360 RPM (b), vertical center linear measurement (c), as well as the corresponded target sample (d). 32

Figure 3.9. End mill tool phase-shifting raw image from location 1~6. 34

Figure 3.10. End mill tool phase-shifting geometry expanded panorama surface map (a) and the vertical wave-fall map (b). 35

Figure 3.11. Dinosaurs-patterned wood rolling pin. 36

Figure 3.12. End mill tool phase-shifting raw image from location 1~5 36

Figure 3.13. Dinosaurs-patterned rolling pin whole view reconstruction results, stitched geometry expanded surface map (a), the reconstructed 3D rolling pin map(b) and the top view map (c). 37

Figure 4.1. Fluid media effects on the cylindrical surface 42

Figure 4.2. reflection effect on plastic wrapped barcode target[82]. 44

Figure 4.3. Fluorescent-reflective fluid fabrication (left) and stokes shift effect (right). 45

Figure 4.4. Principle of fluorescence strobo-stereoscopy: (a) experiment set-up and schematic diagram (b) single image reconstruction comparison on an ø1" rod under with and without fluorescent fluid conditions 47

Figure 4.5. Imaging results of the normal LED and UV light with fluorescent liquid for rough and polished surface comparison. 49

Figure 4.6. 1'' Dia. rod surface reconstruction comparison among stereoscopic, Alicona confocal microscope in the surface map and the horizontal scan. 50

Figure 4.7. 1'' Dia. rod surface reconstruction vertical linear scan results comparison among stereoscopic, Alicona confocal microscope and profilometer results 51

Figure 4.8. Comparison of SS and FSS imaging surface map results 52

Figure 4.9. Comparison of SS and FSS imaging linear scan results 53

Figure 4.10. A full field of 3D FSS image reconstruction process of a target rotating at 30 rpm 55

Figure 4.11. A full field of 3D FSS image 56

Figure 4.12. A full field of 3D SS image 56

Figure 5.1.Surface profile, waviness, roughness components based on frequency distribution [116]. 63

Figure 5.2. ISE process flow chart 64

Figure 5.3. Feature-selective segmentation and merging: flow chart (left) and preliminary experiment results (right). 66

Figure 5.4. Experimental setup for stereoscopic 3D imaging. 68

Figure 5.5. 3D imaging results: FSS, bandpass-filtered, gaussian-filtered 3D images 69

Figure 5.6. 3D imaging horizontal linear scan results: FSS, bandpass-filtered, gaussian-filtered 3D images 70

Figure 5.7. Experimental setup for strobo-stereoscopic 3D imaging. 71

Figure 5.8. FSS-applied strobo-stereoscopic 3D image: full-view image (top) and A-A' profile (bottom). 73

Figure 5.9. 3D strobo-stereoscopic image reconstruction results: isometric view (left) and top view (right). 74

Figure 5.10. FSS-applied strobo-stereoscopic 3D image: full-view image (top) and A-A' profile (bottom). 75

Figure 5.11. 3D strobo-stereoscopic image reconstruction results: isometric view (left) and top view (right). 75

Figure 6.1. Summary of the proposed machine vision techniques in this dissertation..... 77

Figure 6.2. Strobo-Stereo-Spectroscopy technique methodology. 79

Figure 6.3. Dual mode structure light based multi-channel stereoscopy......................... 80

Figure 6.4. Adaptive single stereoscopic feature extraction system................................ 82

LIST OF TABLES

Page

Table 1.1 capability of summarized metrology methods for four criteria in automated mass production in-line analysis 8

Table 3.1 Vertical linear measurement results under different working RPM 33

Table 4.1. Linear scanned comparison results 54

Table 4.2. Linear Zeiss CMM, SS and FSS measured results comparison 57

1. INTRODUCTION

In this chapter, criteria for surface quality inspection and the existed surface metrology techniques are reviewed in Sec. 1.1. The research motivation is presented in Sec 1.2. The dissertation overview is described in Sec 1.3.

1.1. Current Surface Quality Inspection System

The Fourth Industrial Revolution, known as Industry 4.0[1], conceptualizes rapid change to technology, industries, and societal patterns and processes in the 21st century due to increasing interconnectivity and smart automation[2]. Maximizing collaboration productivity to be adapted to this rapidly changing world, globalization, customized mass products and automation process[3] is the ultimate goal for industry 4.0.

This concept aims to create smart or intelligent manufacturing, metrology, supply chains and products [4-6], and also to link the industry to the information technology, as well as all associated activities[7].

(1) smart manufacturing[8,9]: the use of data analytics and new manufacturing techniques and technologies (such as autonomous robots, multi-purpose production lines and augmented reality) helps to improve quality and accelerate production. This enables new business models such as mass customization.

(2) Smart metrology[10-13]: the implementation of a revised metrological function to make relevant decisions with the support of emerging digital technologies. This requires the metrology system to be autonomous, flexible, high productive, and self-adaptable to

the fabrication line. This enables the business models with in-time monitoring and can further reconfiguration of a production process.

(3) smart supply chains and products[14-16]: the intelligent data acquisition and analysis about the products, flow of information, feedback from customers and market in real time, thus enabling tracking of products attributions in an integrated business planning model to challenge the changing of environment. This also enables remote diagnostics and predictive maintenance and can optimize the operating condition.

1.1.1. Metrology requirements for automated mass production

Metrology is always the challenge to warranty the quality of parts. Nowadays, the metrology development requirements are related to the trustworthiness of measurement in different scales, timeliness and security of the connection to a data processing unit and forming the predictions of the course of the process analyzed[17].

Figure 1.1 summarize the common inspection applications during the manufacturing process. For automated mass production specifically, it requires high-speed and instantaneous analysis, with the field of view (FOV) varied from millimeter to meter range and down to 1millimeter range of depth uncertainty. Four main criteria, surface quality examination, target locating, high-speed instantaneous or fast analysis, flexible metrology-in-loop with fabrication line, are shown in this figure as well.

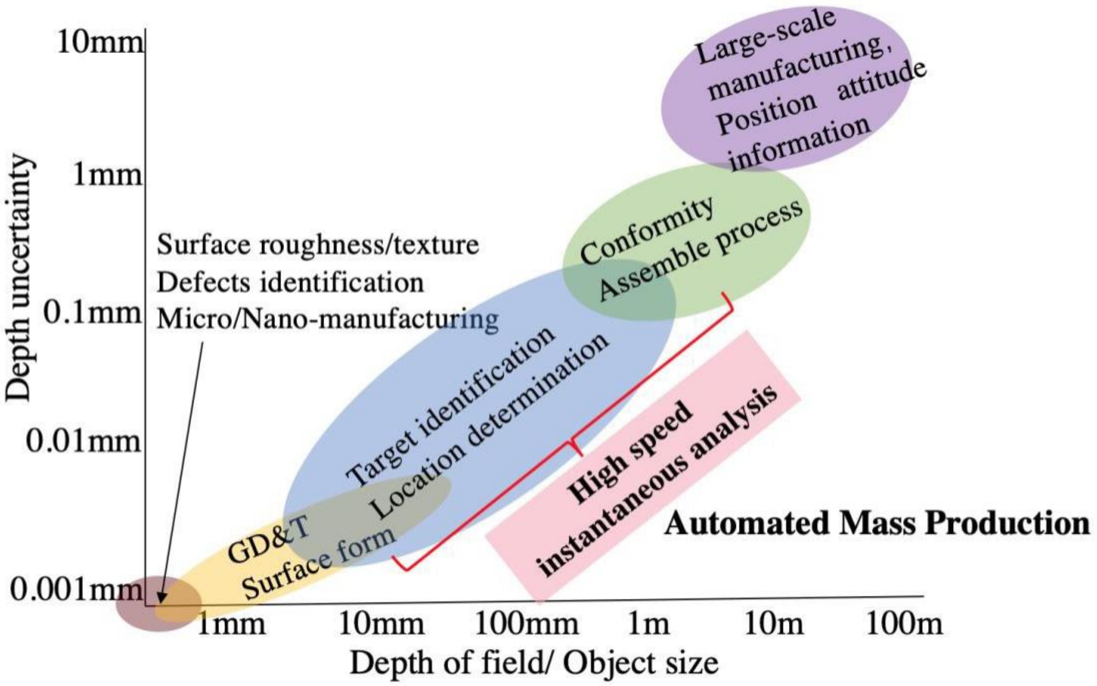

Figure 1.1 Applications distribution for process control during the manufacturing based on the Depth of field/Object size and Depth uncertainty.

For most of the products, the surface profile monitoring, surface form metrology, target identification and location determination are the fundamental objectives through the process control. For the integral metrology system, two most challenging issues exist[18], which are high-speed in monitoring and inspection, flexible in the imbedded metrology-in-loop system.

For the "high-speed", on the one hand, it requires faster measurement processes for the rapid provision of information[19], on the other hand, it requires the integration of measurement technology into production processes, particularly by means of automation[7].

For the “flexibility” is the key factor to link manufacturing industry to the information technology. Individualized products require a corresponding adjustment of processes, which means that production facilities are frequently reconfigured and associated changes in production control operations are necessary[20, 21]. These changes must be implemented efficiently for economy efficiency for the real world, where the metrology plays an essential role.

1.1.2. Surface quality inspection techniques

Surface metrology can be categorized as contact profilometry and non-contact profilometry, while the second includes the displacement method and the non-contact optical methods. In the same way, Figure 1.2. summarizes the corresponded metrology techniques distribution among the depth of field /object size and depth uncertainty.

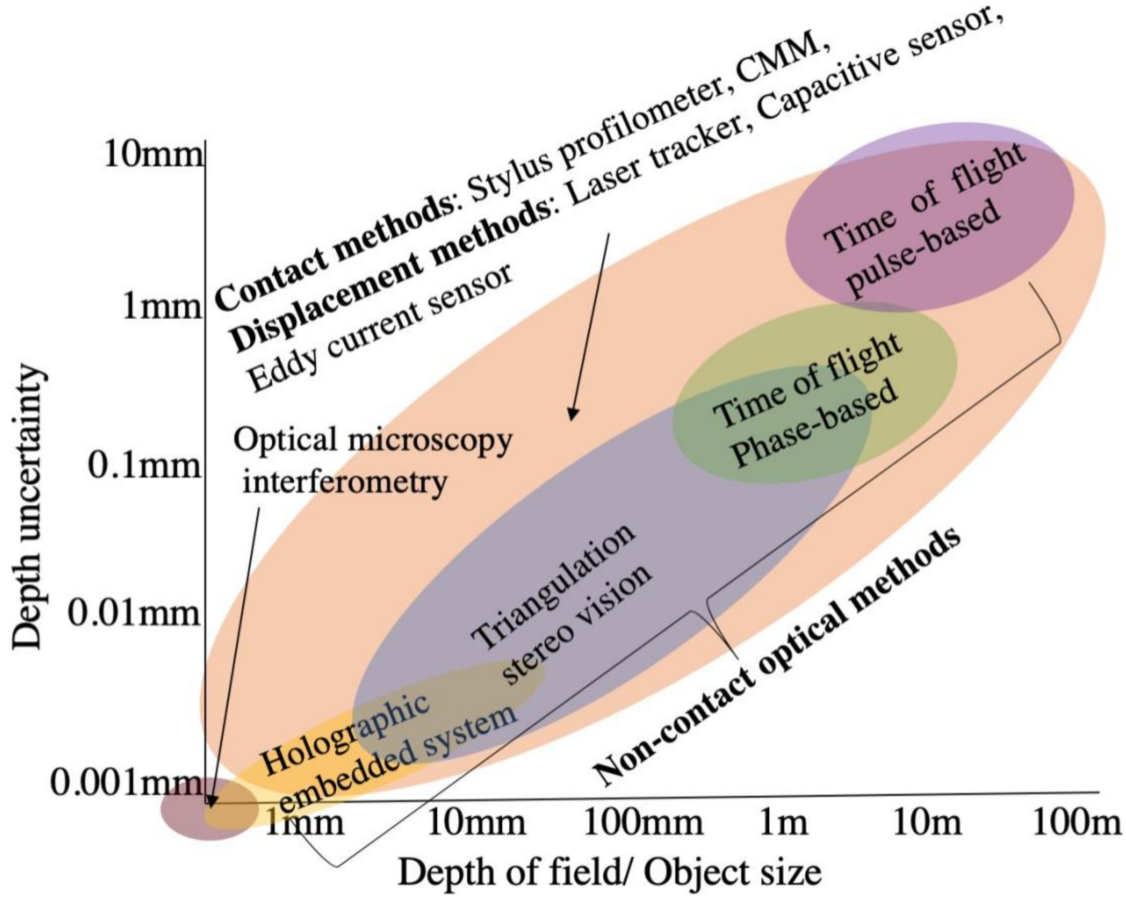

Figure 1.2 Applications distribution for common surface metrology techniques based on the Depth of field/Object size and Depth uncertainty.

Contact profilometry[22] is widely accepted and has been used for many decades in manufacturing field for arbitrary surface profile measurement. It normally uses stylus type devices, which correlate the vertical displacement of mechanical, electrical or optical transducers, to scan along the surface. The resolution can be in atomic scale when atomic force microscope[23] is used. The disadvantages are obvious, as this method requires direct physical contact with the surface of the workpiece, the test surface can be potentially damaged, also, the measurement time is relatively long for excellent lateral resolution. Therefore, it is not suitable for high-speed and high-volume production systems.

Non-contact profilometry involves with displacement sensor related techniques, such as laser tracker, capacitive sensor, eddy current sensor, and optical profilometry. The type is flexible on the object size, however, as either reference ball is included or involves with the limitation on materials and the displacement between the sensor and the target sample, the metrology time is long as well and the resolution is related to the reference ball size or the sensor size.

Optical profilometry in the precision metrology includes microscopy and interferometry. Confocal microscopy is first described by Minski in 1957 [24,25] and applied in the surface characterization. Surface roughness and profile can be measured with high vertical resolution with large numerical aperture($0.6<NA<1.4$)[26,27], 3D reconstruction can be achieved in micro-scale[28], reconstruction in large field of view can be finished with stitching process. This technique is still single point detection, the speed of data acquisition is a limiting factor.

Interferometry utilizes the wave nature of the light to achieve high accuracy measurement by detecting the optical path length difference between reference surface and test surface[29].Modern interferometers apply white light instead of monochromatic light for high steep surface, as it distinguishes discontinuity of the surface for example deep valleys or high steps[30]. This avoid the using of computer-generated hologram (CGH) [31,32] as null optics in classic interferometry. Still, stitching process is required for mm range of measurement. All these developed non-contact methods are off-line-based, because of the requirement for environment stability and long processing time.

Triangulation based machine vision systems are based on capturing images (typically via cameras), extracting a series of data from images, making a decision according to the analyzation[33]. This method is promising for on-machine monitoring processes because of its cost-effective data acquisition devices, along with emerging technologies in fast image processing and computer vision. 2D image analysis studies have been carried out for the assessment surface texture and roughness. These methods are based on statistical analyses of the gray-scale images in the spatial domain [34]. A 2-D fast Fourier transform (FFT) of the digitized surface image in which the magnitude and frequency information obtained from the FFT are used as measurement parameters of the surface finish has developed by Hoy and Yu [35]. Ashour et al. [36] presented a study on the classification of different types of machining using histogram-based features.

3D image reconstruction techniques based on triangulation, like stereoscopy and structure light. Comparing with 2D analysis, 3D analysis is less sensitive to the illumination intensity variation, and more accurate in the dimension as the depth information can be directly calculated instead of assuming the targets are in a flat surface[37]. Krishna et al.[38] proposed surface topography characterization using 3D stereoscopic reconstruction of SEM images pair. Hu et al.[39] discussed the relationship of roughness parameters calculation process under stereoscopic algorithm based on ISO standard. Unsupervised defects detection and categorization in railway[40], concrete [41], PCB board [42] and welding industry[43-44] have been well reported.

Time of flight techniques detect direct displacement between the sensor and object. It based on the time difference between the emission of a signal and its return to the sensor after being reflected by an object. Because of this, it is widely applied on the large-scale metrology, and the vertical resolution is low as it can be shown in the Figure 1.2.

Table 1.1 summarized the discussed the capability of existed surface metrology methods for in-line analysis.

Table 1.1 capability of summarized metrology methods for four criteria in automated mass production in-line analysis.

	Contact method, or displacement methods	Microscopy, interferometry	Triangulation stereo vision	Time of Flight Technique
Surface quality	moderate	easy	moderate	difficult
Target location	easy	moderate	easy	easy
Fast analysis	difficult	difficult	easy	difficult
Metrology -in-loop	difficult	moderate	easy	difficult

From the discussion above, in-process metrology system is required for the automated mass production inspection. On-machine or in-process metrology means the measurement of the work-piece surface carried out on a manufacturing machine where the workpiece is manufactured[45].

Measurement systems for on-machine and in-process surface metrology can be classified into probe-scan systems and full-field systems. As we discussed above, the probe systems cost long measurement time, also, such systems involve with the uncertainty sources of motion errors of machine axes, probe alignment errors, thermal drift, vibration, etc. [46]. The full-field system, which is usually an optical system, a light beam is projected onto a certain area of the workpiece surface for capturing the three-dimensional (3D) topographic information over an area, which is often referred to as the field of view (FOV) of the system[45]. As the interferometry and the microscopy systems are designed with high cost, difficulties on the mounting process, and sensitivities to the working environment, the triangular based machine vision surface inspection systems match with the requirement for automated mass production inspection. This technique with the ability to detect small defects, monitor the surface profile quality while manufacturing, and categorize desired pattern, it can also provide valuable data that can be used for optimizing processes.

1.2. Motivation

The motivation of this dissertation is to build an integral stereoscopic inspection system for surface quality and feature selection at both single framed location and 360° full-view 3D reconstruction. Machined parts with low and high reflectance are considered as target sample, thus it can track the target performance through different manufacturing status from the ground to polished surface. Feature selection algorithm is investigated for desired structure extraction.

Through this dissertation, we want to provide a solid understanding of the proposed system fundamentals and principles, and practical solutions to different industrial applications. From the engineering point of view, we hope to apply this system on real manufacturing projects to have practical implementation and verification. Figure 1.3. presents the research motivation, objectives and proposed solutions.

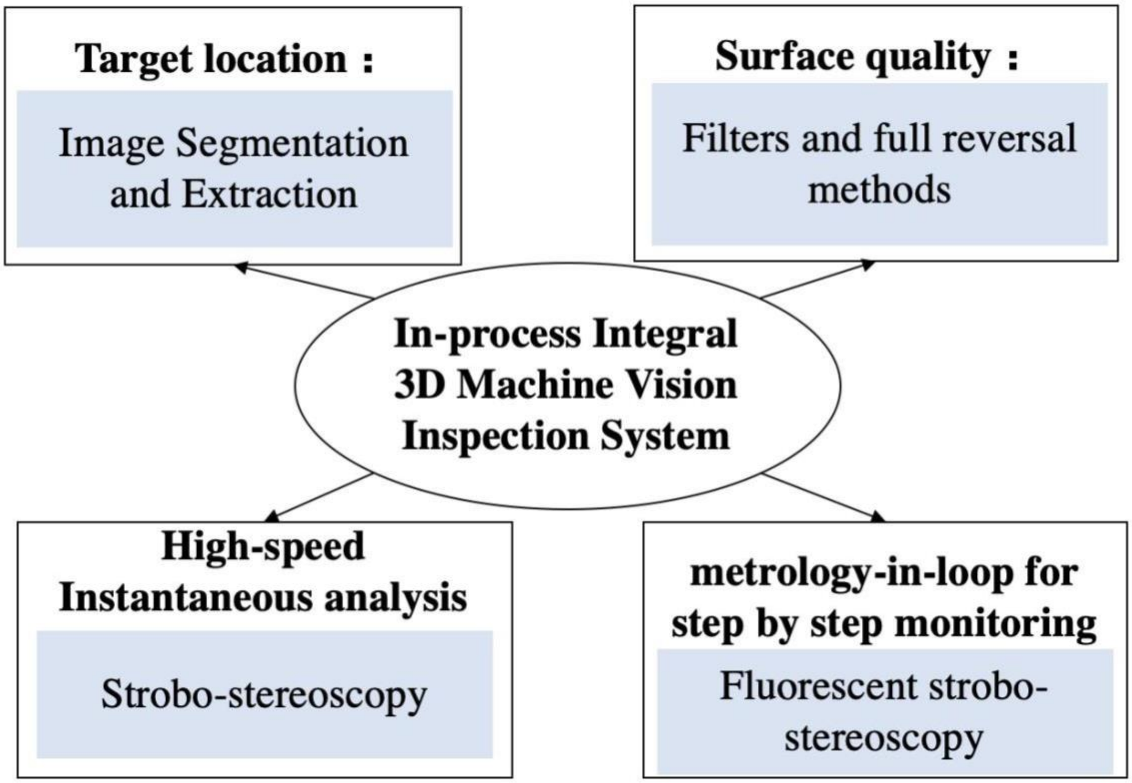

Figure 1.3 Research motivation, objectives and proposed solution.

1.3. Dissertation Overview

This dissertation consists of six chapters. It proposes an on-machine whole view scanning stereoscopic system and summarizes engineering implementation for different metrology projects.

Chapter 2 BACKGROUND describes the test principle of stereoscopy and surface feature extraction techniques based on filtering process. This is the fundamentals of further proposed methods.

Chapter 3 STROBO-STEREOSCOPY proposes a fundamental system for on machine 3D reconstruction and examination configuration. Experiments were performed on a 2’’ diameter patterned roll and a 3/8’’ diameter micro mill tool to prove the capability. A 1’’ machined cylinder target was applied for a machining process monitoring, surface profile on each status was examined, geometric dimension and tolerance like cylindricity, roundness axis straightness were measured as well.

Chapter 4 FLUORESCENT STROBO-STEREOCOPY provides an implemented strobe-stereoscopy method for high reflectance surface. The effect comparison with fluorescent liquid and with different intermedia on 1’’ cylindrical target was provided. A test system utilizing this method for 2’’ patterned aluminum coated surface was presented at the end of this chapter.

Chapter 5 FEATURE SEGMENTATION AND EXTRACTION TECHNIQUE describes a filtering process based automated feature segmentation and extraction technique for 3D surface map. This technique can extract the desired structure information from the random base structure. The experiment on 1mm and 0.1 mm round shape patterns extraction was presented.

Conclusion and further implementations are given in Chapter 6.

2. STEREOSCOPY METROLOGY OVERVIEW

In this chapter, the fundaments of stereoscopy metrology are introduced. The history of stereoscopy is reviewed in Sec. 2.1. The principle of stereoscopy is described in Sec 2.2. The current applications and challenges are summarized in Sec 2.3.

2.1. History of Stereoscopy

Stereo vision is motivated from the human vision system, which can perceive depth properties of a pair of images. The stereoscope was first described and invented by Sir Charles Wheatstone in 1838[47] for entertainment, astronomy and geography observation. The first stereoscopic observation of moon surface was finished in 1858 [48].

The modern computational solutions for stereo vision problems involves six steps: image acquisition, camera modeling, feature acquisition, image matching, distance (depth) determination, and interpolation[49]. Stereoscopic images can be acquired in various ways based on the application to determine the field of view, resolution, illumination and so on. Camera model is related to the coordinate systems of two cameras and the target scene and the distortion removal with the captured image pairs. Feature acquisition and image matching is to match the elements of the target in the left and right image pairs, featureless areas of nearly homogeneous brightness cannot be matched with confidence[50]. Once accurate matches have been found, the determination of distance will be a relatively simple matter of triangulation. Interpolation is to match the reconstruction depth matrix from a sparse array to a dense one when the depth map is not complete enough to capture the important changes in depth.

2.2. Stereoscopy Principle

The common type of the stereoscopy technique is embedded with two CCD (charge - coupled device) or CMOS (complementary metal oxide semiconductor) cameras capturing images located bilaterally symmetrically regarding the target. The 3D scene is reconstructed by the location information of the same object points from both the left and right images. Figure 2.1 shows the principle of the stereoscopic imaging process.

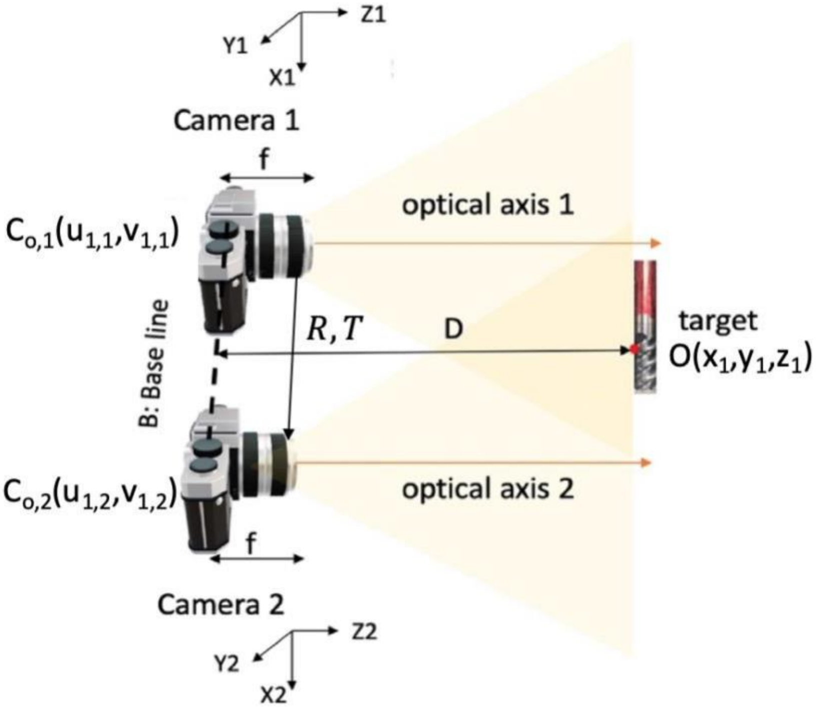

Figure 1.4. Stereoscopic system principle[51].

Camera 1 and 2 with their own coordinate system and same f, which is the focal length of the lens system, B is the base line and D is the measured distance from the point O on the target to the CCD of the camera system. According to the triangulation and lens equation, where

$$D = f\frac{B}{y_2-y_1} - 1 \tag{1}$$

To understand the stereo geometry, a direct calibration method is presented to obtain geometric relationship between two stereo cameras, which can be done by 3D Euclidean transformations, rotation R and translation T. The projection of three-dimensional points (X_m,Y_m,Z_m) onto the camera sensor $(u_{(n,m)},v_{(u,m)})$is described by [52]

$$S_m \begin{bmatrix} u_{n,m} \\ v_{n,m} \\ 1 \end{bmatrix} = K_n \begin{bmatrix} R_n & T_n \\ 0 \quad 0 \quad 0 & 1 \end{bmatrix} \begin{bmatrix} x_m \\ y_m \\ z_m \\ 1 \end{bmatrix} = P_n \begin{bmatrix} x_m \\ y_m \\ z_m \\ 1 \end{bmatrix} \tag{2}$$

$$K_n = \begin{bmatrix} f_u & 0 & u_0 \\ 0 & f_v & v_0 \\ 0 & 0 & 1 \end{bmatrix} \tag{3}$$

where $(u_{(m,n)}$, $v_{(m,n)}$) are the pixel coordinates of the point m in camera n, S_m is a normalization factor, K_n is the intrinsic matrix for camera n, R_n and T_n are the rotation and translation matrices of camera n, P_n is the camera projection matrix and (X_m , Y_m , Z_m) are the coordinates of point m. f_u and f_v describe the focal length of the lens in the u and v direction respectively and u_0 and v_0 are the pixel coordinates of the intersection of the optical axis with the imaging plane.

Almost all camera lenses have distortions. Distortion is magnification error varying with image height which maps straight lines in the objects to be curved lines in the camera image. Brown's model [53-55] is a common model describing camera distortion in computer vision which includes radial distortion, decentering distortion and thin prism distortion, which arises from imperfection in lens design and manufacturing as well as camera assembly. Due to camera distortion, the image coordinate is shifted from its ideal position so that

$$u_{d(m,n)} = u_{(m,n)} + \delta u_{(m,n)}$$

$$v_{d(m,n)} = v_{(m,n)} + \delta v_{(m,n)} \tag{4}$$

$u_{d(m,n)}$ and $v_{d(m,n)}$ are distorted point coordinates, $\delta u_{(m,n)}$ and $\delta v_{(m,n)}$ are the amount coordinate shifts due to lens distortion. For radial distortion, it is defined as

$$\delta u_{(m,n)} = u_{(m,n)}(k_1 r^2 + k_2 r^4 + k_3 r^6 + \cdots)$$

$$\delta v_{(m,n)} = v_{(m,n)}(k_1 r^2 + k_2 r^4 + k_3 r^6 + \cdots) \tag{5}$$

where k_1, k_2, k_3 are the radial distortion coefficients, $r^2 = u^2 + v^2$.

Decentering distortion arises when the center of the lens elements are not aligned collinear. It is modelled as

$$\delta u_{(m,n)} = 2p_1 u_{(m,n)} v_{(m,n)} + p_2(r^2 + 2{u_{(m,n)}}^2)$$

$$\delta v_{(m,n)} = p_1(r^2 + 2{v_{(m,n)}}^2) + 2p_2 u_{(m,n)} v_{(m,n)} \tag{6}$$

where p_1, p_2 are the decentering distortion coefficients.

Thin prism distortion is due to the tilt of lens element or CCD sensor in the manufacturing or assembly of the camera. It can be expressed as

$$\delta u_{(m,n)} = s_1 r^2$$

$$\delta v_{(m,n)} = s_2 r^2 \tag{7}$$

where s_1, s_2 are the prism distortion coefficients. Let $q_1 = p_1 + s_1$ and $q_2 = p_2 + s_2$, we have[56]

$$\delta u_{(m,n)} = 2u_{(m,n)}(p_2 u_{(m,n)} + p_1 v_{(m,n)}) + \ q_1 r^2$$

$$\delta v_{(m,n)} = 2v_{(m,n)}(p_2 u_{(m,n)} + p_1 v_{(m,n)}) + \ q_s r^2 \tag{8}$$

The distortion effect in Eq.(8) is illustrated in Figure 2.2.

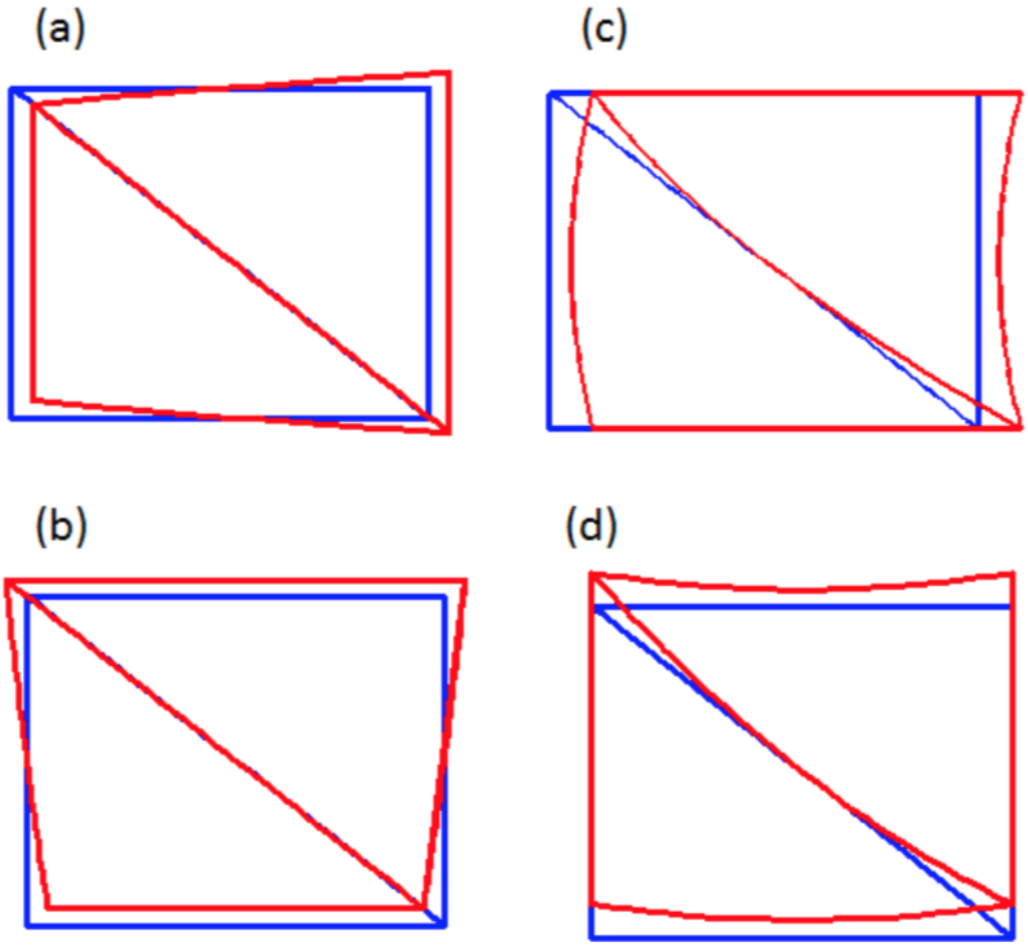

Figure 1.5. Effect of lens distortion. (a) and (b) show the effect of p_1 and p_2 , where p_2 = 0 in (a) and p_1 =0 in(b).(c)and(d)show the effect of $q_1$and q_2 ,where q_2 =0in(c)and q_1 =0 in(d)[57].

Usually the dominated camera distortion is first-order radial distortion, which corresponds to k_1 in Eq. (5), the effect can be seen in Figure 2.2.

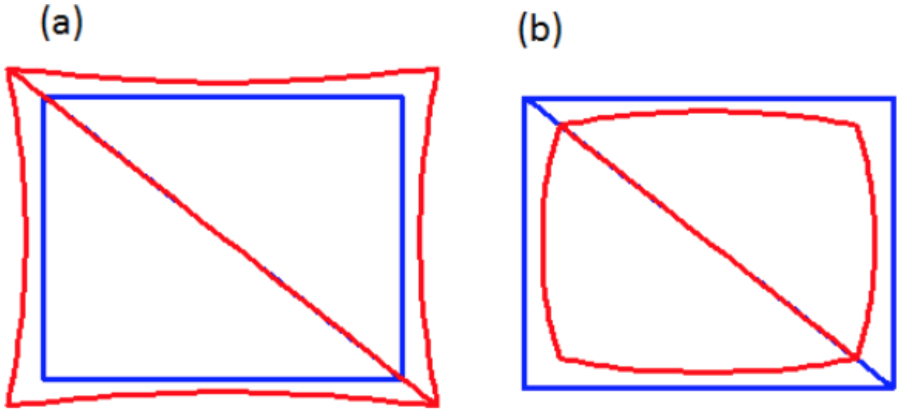

Figure 1.6. Effect of camera radial distortion k_1, (a) k_1 is positive (b) k_1 is negative[57].

Image matching algorithms can roughly be classified into two categories:

(1) Area based matching[52]. In this category, the algorithms attempt to correlate the intensity of grey levels of image patches, assuming that they present some similarity. The underlying assumption appears to be a valid for relatively textured areas and for image pairs with small difference.

(2) Feature matching[56,58]. In this category, the algorithms first extract salient primitives from the images, such as edge segments or contours, and match them in two or more views. Common techniques are tree searching, relaxation, maximal clique detection, etc. Some heuristics such as assuming affine transformation between the two images are usually introduced to reduce the complexity.

The overall calibration has been performed using images of a predefined calibration grid. Specific points were extracted to obtain a sufficient number of combinations (pixel, 3-D point) to determine the previous introduced intrinsic and extrinsic camera parameters or the projection matrix coefficients of the system [38]. These parameters transfer the scene points in 3D space to their corresponding image points, thus the measured depth can be recovered.

In this study, calibration was performed with the same camera systems for the target sample measurement. The Stereo Camera Calibrator app in MATLAB was applied to the calibration process.

2.3. Stereoscopy System Applications, Design criteria and Challenges

a Stereoscopy system is often used to accomplish the following tasks: object recognition; surface shape and size detection; product processing and assembly; around the obstacle avoidance and navigation[59]. The measurement range is from micro scale to macro scale. Stereo-microscopy [32,60-62] was proposed for surface roughness, wafer pattern measurement based on scanning transmission electron microscope (SEM) or traditional microscope. For large field of view from mm to m range, automated monitoring techniques was developed for automobile or aircraft assembly process[63-65]. Imaging online inspection options are also provided to determine the quality of pharmaceutical, or electronics parts [45,66]. By feature detections of obstacles and signals, it can also help guidance for autonomous navigation[67,68].

The main criterion in stereo system design is to recognize that the part is well made according to the specified qualifications[36]. The scene specifications, environment, and all the constraints must be considered in the design as this determine the lighting condition. The types of materials, limitations in the range of positions of target objects are important as it constrains the camera and lens system selection, along with image acquisition location.

Metrology with stereo vision is a non-contact solution to a board range FOV target inspection and is convenient to be embedded to the existed manufacturing. Challenges like cost in high-speed mass measurement, high reflective surface measurement, and system with metrology-in-loop remain to make advanced 3D shape measurement techniques accessible and available to solve challenging problems in science, engineering, industry, and our daily lives[69].

Although the use of off-the-shelf components has brought down the cost of most 3D imaging, when it comes to apply one-size-fits-all approach in high speed and mass production often require prohibitively expensive customizations.

Difficulties to measure high specular surfaces are always a challenge as such surfaces introduce “false” images into the camera systems. Typically, additional equipment, such as polarizers or special arrangements, and adaptive illumination design are required [70-71]. The implementation of these additional procedures or equipment reduces flexibility for measuring other surfaces. As discussed earlier, recent developments have opted for specialized codification approaches to avoid the use of additional hardware [72], this also increase the measurement time.

The needs for system metrology-in-the-loop become critical for an industry such as additive manufacturing because each layer should be inspected before moving to the next layer. It is even better if the machine can make adjustments on the next layer based on the current layer’s information. This goal may be achieved if 3D surface metrology is embedded into the manufacturing process such that in situ measurement, in situ data analytics, and in situ decision making can occur while the part is being made. One of the most challenging issues is that the software/hardware latency could undesirably slow down the production process.

3. STROBO-STEREOSCOPY*

To directly monitor the information of machine tool and machined parts during the manufacturing process, this chapter presents a novel 3D imaging technique which combines stroboscopy and stereoscopy. By synchronizing the stroboscopic illumination system with the spindle control system, this technique enables in-situ 3D reconstructing of rotating parts including machine tools.

Sec 3.1 introduces system methodology and calibration procedures. Then, the system setup and initial measurement results are presented. A whole view 3D reconstructions process is in Sec 3.3. These results verify the capability of the geometry identification of the proposed strobo-stereoscopic imaging technology. Lastly, the potential applications of the proposed technology were discussed.

3.1. Stroboscopy Effect

Stroboscopic effect is a visual phenomenon caused by aliasing. It can be used for visual analysis of objects in periodic, high-speed continuous motion. Objects in rapid periodic motion can be studied by using the stroboscope to produce an optical illusion of stopped or slowed motion[73].When the flash repetition rate of the stroboscope is exactly the same as the object movement frequency, or an integral multiple thereof, the moving object will appear to be stationary. This is called the stroboscopic effect.

Along with the modern machine vision techniques, it is possible to perform real-

---

* Reprinted with permission from “Preliminary study of phase-shifting strobo-stereoscopy for cutting tool monitoring” by Xiangyu Guo, ChaBum Lee, 2021, Journal of Manufacturing Process,Vol.64, 1214-1222, © 2021 The Society of Manufacturing Engineers. Published by Elsevier Ltd. All rights reserved.

time measurement of high-speed motion if a hardware system is employed to execute the subsequent-data processing.

3.2. Strobo-Stereoscopy Methodology

The proposed method is illustrated in Figure 3.1 with a patterned roll example. The operation principle is as follows: While stereoscopy is applied for target 3D model reconstruction at specific positions, stroboscopy has two operational modes that enable on-machine whole-view scene construction. When synchronizing the light source illumination frequency and the motion of the object, the object appears to be stationary, and this is the phase-locked mode. If minor differences are added to the frequency, the object appears to be slowly moving or rotating. This slow-motion can be working as the source for the phase-shifting mode. With this phase information, the target can be whole-view 3D reconstructed by 360 degrees.

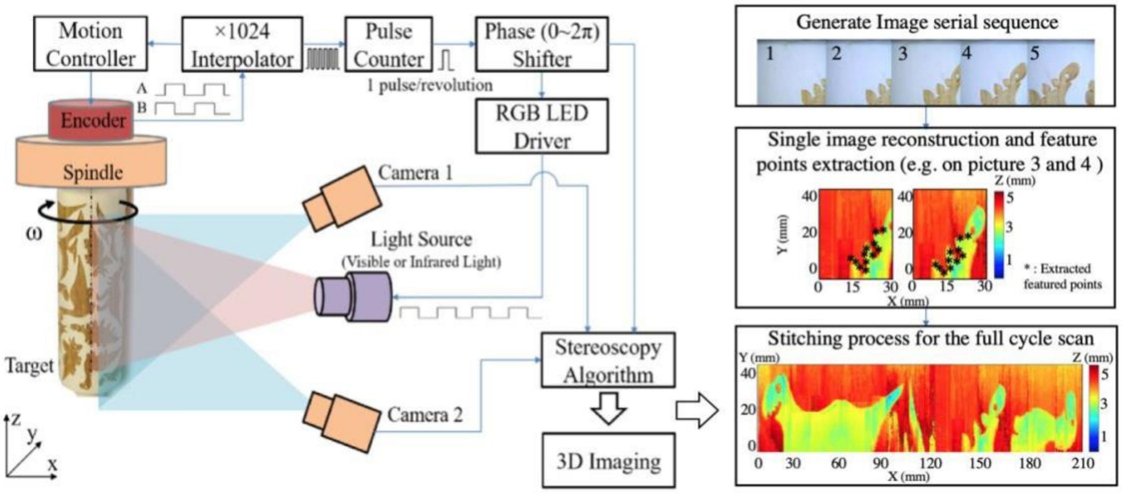

Figure 3.1 Strobo-stereoscopy methodology.

The target rotates at a set frequency ω, and the motion control's pulse counter is used to control the stroboscopic light, which illuminates the cutting tool's specific area by blinking the input LED (light-emitting diode) light. A motion controller can be used tosynchronize and program the illumination system, camera system, and spindle system. Digital signal processing automates measurement operations.

To eliminate system noise, the center surface is reconstructed using a stereoscopic algorithm in conjunction with Gaussian filtering and 3D clustering techniques. Alternatively, super-pixel image reconstruction will be used. During the neighbor surface stitching process, the SIFT (scale-invariant feature transform) method will be used to determine similar characteristics. In conjunction with the rotating angle, the panorama surface can be generated. To align the depth data and eliminate stitching errors, a surfacephase unwrapping process is used.

The patterned roll will be measured and reconstructed first under various rotating speeds in order to determine the optimal working speed condition and demonstrate the 3D whole-view reconstruction capability. Following that, mill tools will be measured in that condition to determine the geometry shape. Finally, the mill tool with embedded tool bits will be monitored under a variety of operating conditions.

3.3. Synchronizing the Flash of Stroboscopic Light with the Motion of the Rotating Objects.

The rising edge of the Encoder index (Z) signal is used as the signal that the whole cycle of rotation is finished. This signal is related to the rotational speed (RPM), and F is the desired LED blink frequency in Hz. When F is equal to the spindle rotary frequency, both CCDs gather pictures at the single location of the cutting tool. This is also called as the phase-locked mode. When F is different from the spindle rotary frequency, which means we introduce the delayed time T into the system, a sequence of images was gathered under the phase-shifting process for a whole-view 3D reconstruction, this is called as the phase-shifting mode.

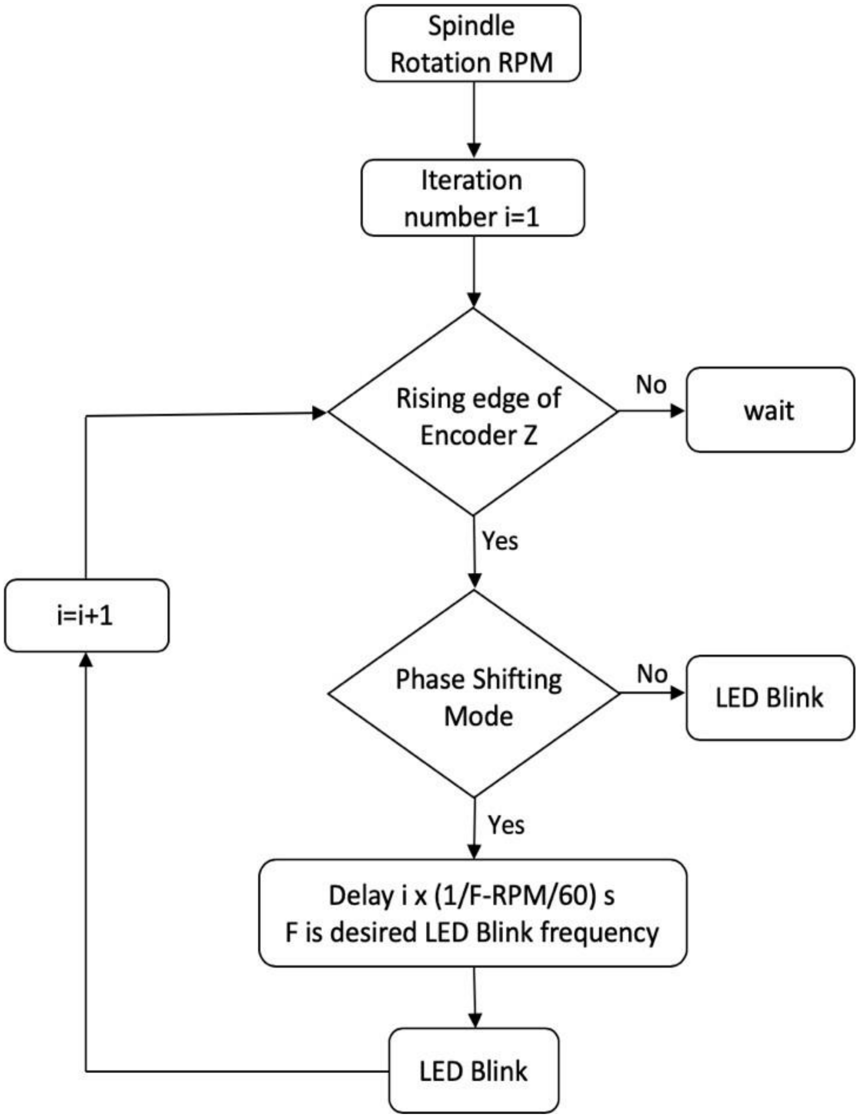

Figure 3.2 Flow chart of stroboscopic motion and light control algorithms. i is a positive integer.

First, the desired number of images per cycle N is set N. The parametric relationship can be expressed as:

$$N = \frac{RPM}{RPM-60F} \tag{9}$$

$$\frac{1}{F} + T = i\frac{60}{RPM} \tag{10}$$

From above, the delayed time information t can be calculated as:

$$t = i\frac{60}{RPM} - \frac{60}{RPM-\frac{N}{RPM}} \tag{11}$$

To gather a whole-view 3D surface map, after the phase-shifting process, a stitching algorithm for the depth map reconstruction is required. The full view 3D surface building process was illustrated to explain the depth map reconstruction process as seen in Figure 3.3.

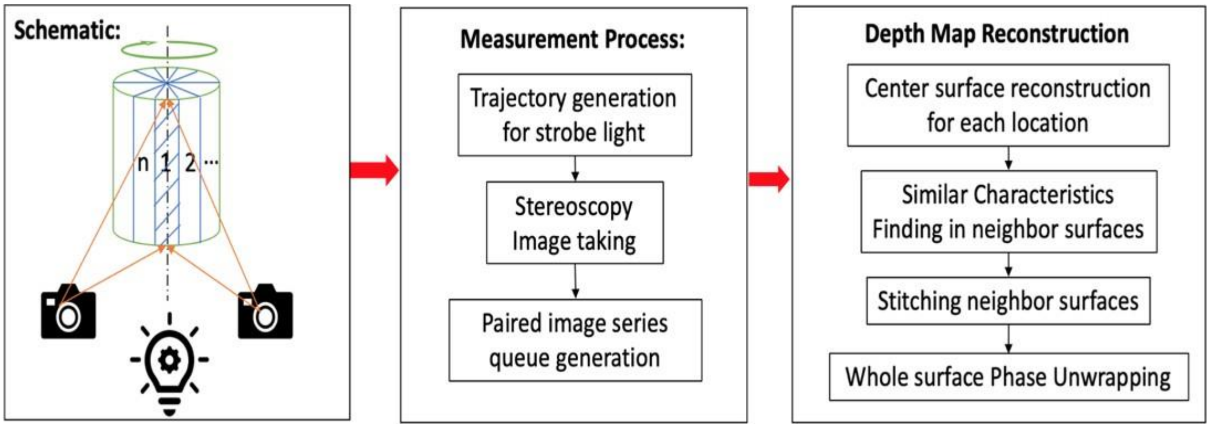

Figure 3.3 Whole view 3D surface building process.

The phase-locked and phase-shifting algorithm synchronizes the rotational speed RPM (revolution per minute) with the light blinking frequency and shifts the phase of the light signal from 0 to 360 degree. Stroboscopic control board is designed, manufactured, tested, and installed in a computer. The unit has two control modes: phase locked and phase shifting mode. The trigger signal is related to the encoder signal Z to flash the LED and capture an image pairs according to a frequency set in advance through software.

Though the stroboscopic effect can "freeze" the in-motion objects, the exposure time can still cause the blurring of the images. Theoretically, the shorter the exposure time of the camera and the pulse width of illumination are, the sharper the image will be, but a shorter exposure will depress the contrast of the images. To balance the image accuracy, pulse width ratio is selected for different rotating RPM.

3.4. 3D Surface Reconstruction

A 3D printed reference array with 4 mm diameter and 4 mm height cylinders on was applied as the reference target to prove the 3D surface reconstruction process. The target is shown in Figure 3,4. The reconstruction process on one of the cylinders is in Figure 3.5.

Figure 3.4. 3D Printed reference array.

The 3D reconstruction is based on the stereoscopic method, the working principle is shown in Figure 3.5 (a). After gathering the depth map, tip/tilt (this information could be observed in Figure 3.5 (c) depth map and noise information would exist in the raw image. The system error removal process was applied to remove the unbalanced information from the reconstruction depth map Figure 3.5 (d). The gaussian filter is applied to decrease the noise level and smooth the surface map. Once the surface map was achieved, the validation was performed.

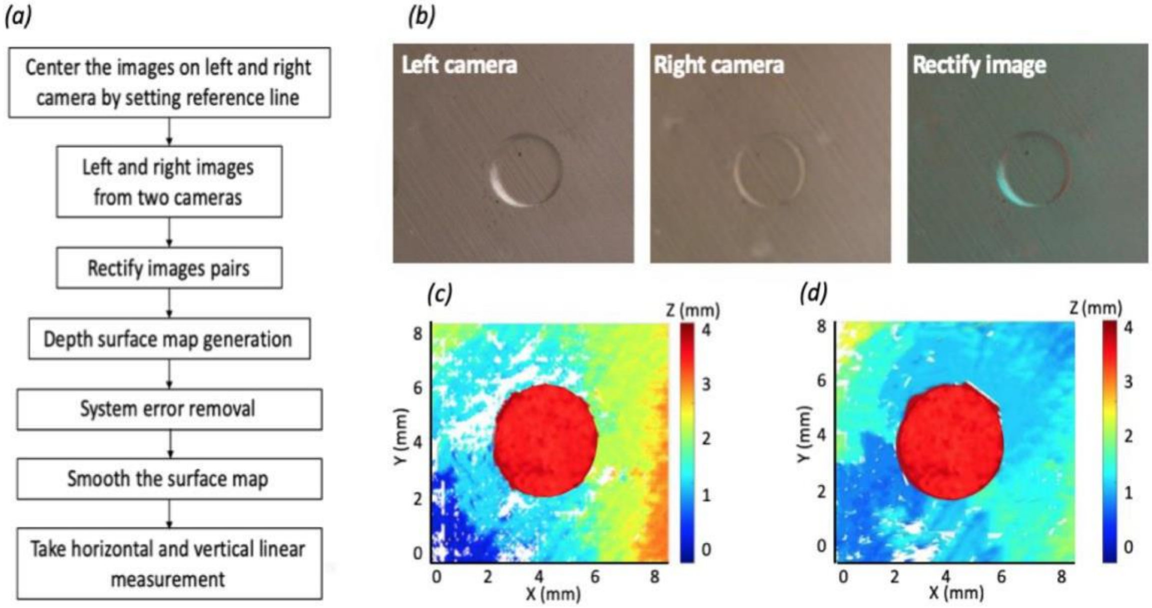

Figure 3.5. Stereoscopic reconstruction process (a), example on stereoscopic reconstruction process (b), depth map(c) and system error removed and filtered map (d).

Linear measurement results are extracted from Figure 3.5(d), which are presented below, where the average value of the height from Figure 3.6 (a) on the proposed method is 4.08 mm. Because the part was 3D printed by fused deposition modeling, the printing patterns were also observed in Figure 3.6 (b). The target linear-scanned results (blue) are compared with the dial-gauge (resolution of 0.001 mm) testing result (orange), as shown in Figure 3.6 (b) as well. Fixed with a motorized linear axis, set the initial dial-gauge value to be 0 when it is at the edge of the target structure, the data was read out every 0.5 mm along the same-measured direction by the proposed method(Figure 3.5 (d)). The dial gauge indicated the height is approximately 4.15 mm, and the height variation can be observed in Figure 3.6 (c).

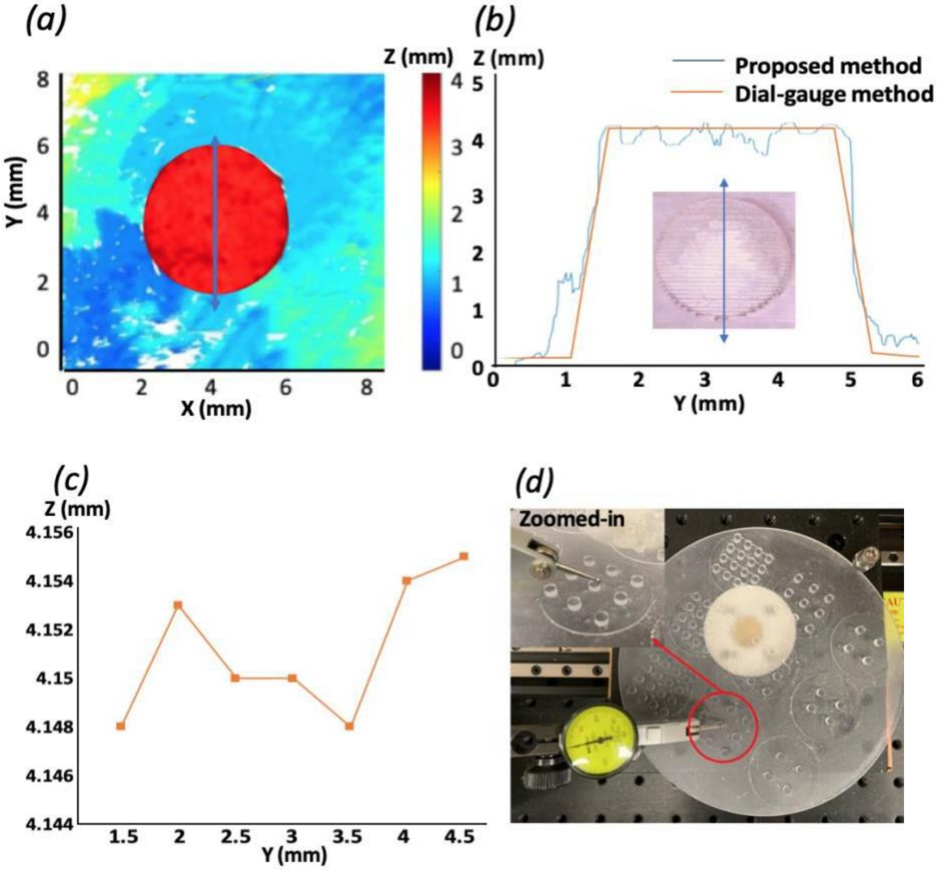

Figure 3.6. 3D printed part surface map (a), the linear extract measurement in the blue arrow line location (b), dial-gauge measured height variation (c), and dial-gauge measurement set-up (d).

3.5. Experiment and Results

3.5.1. Experiment setup

In the proposed system, to minimize the rotational motion error-induced effect, the aerostatic spindle (rotational error < 0.1 μm) with 2048 steps per cycle (encoder signal) was applied, and working under the velocity control mode to secure the motion accuracy and rotational speed. As shown in Figure 3.7 (a), two CCDs (30 frames per second) with the lenses (field of view: 18×24 mm) were installed on two linear rails (x- and z-direction) with rotary stages to capture the raw picture of a cutting tool bit for further 3D reconstruction. Cross lasers on top of each CCD camera were added to guarantee both cameras focus at the exact location of the measurement target. An end mill tool (ø 1/8") was used as the experimental target as seen in Figure 3.7 (b).

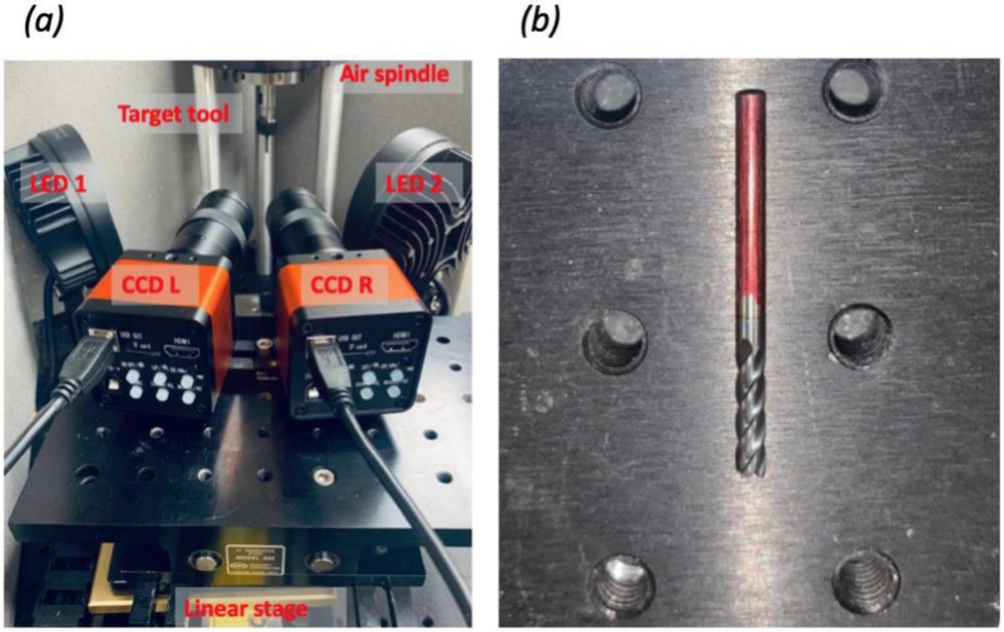

Figure 3.7. Experiment set-up of the proposed method (a) and experiment target end mill tool sample (b).

3.5.2. Phase-locked mode

The developed strobo-stereoscopy measured the cutting tool geometry under 90, 360 RPM. The surface reconstruction maps along with the center vertical linear scanning results were shown in Figure 3.8. In Figure 3.8(c), a 1 mm interval was added to present the results clearly. The similar pattern on the center linear scan can be observed.

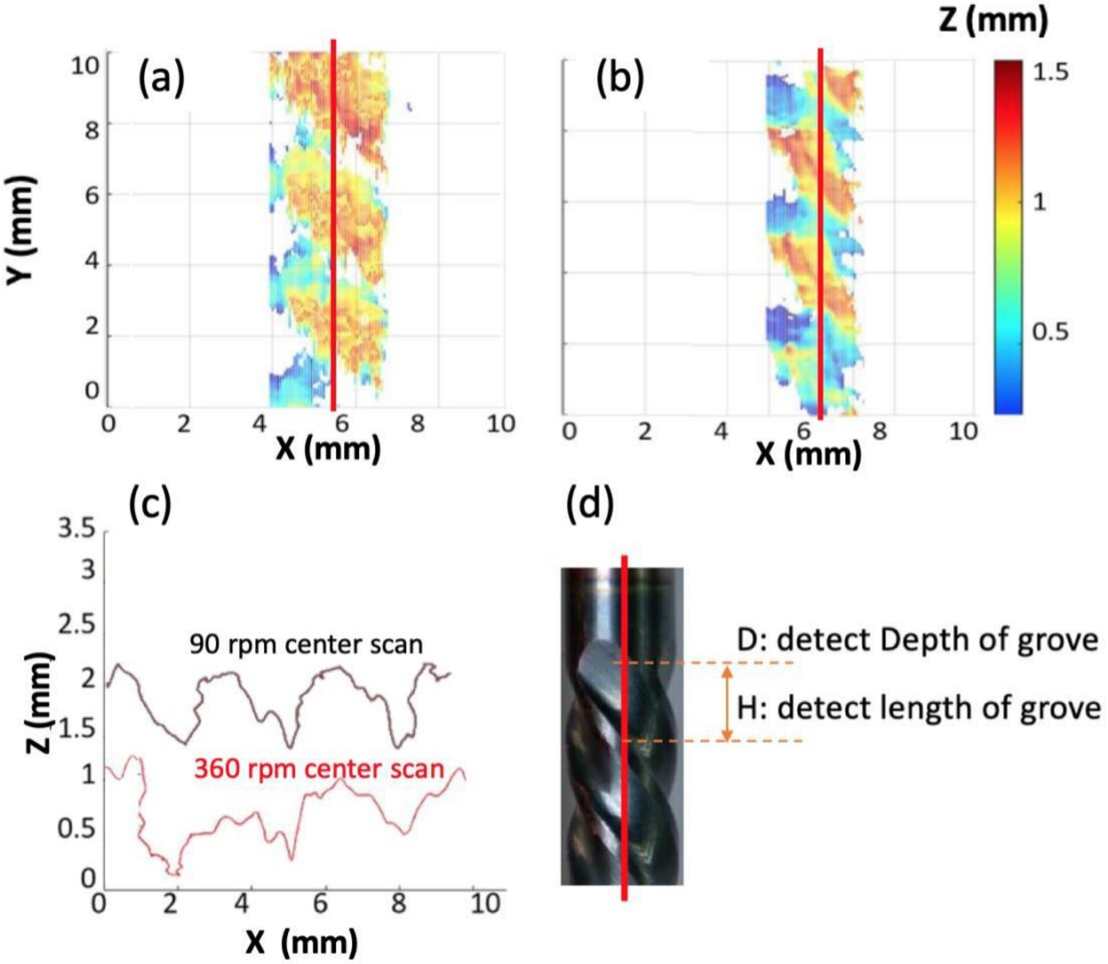

Figure 3.8. End mill tool phase-locked surface map at 90 RPM (a) and 360 RPM (b), vertical center linear measurement (c), as well as the corresponded target sample (d).

For each working condition, 5 raw images were captured, the averaged information from the raw images was used to reconstruct the surface map. The construction process was shown in the previous section. These results provided the ability to measure the surface roughness on the edge and flute. For reference, the white areas on the color maps were induced by the void areas (no reflective areas) and the surfaces with high slope. Most microscopic camera systems have limited performance on the collection of stray light.

Vertical linear measurements were applied on the surface map to validate the surface map reconstruction repeatability. The average values and the deviation values of the detected depth of groves (D) and detected length of groves (H) under each working RPM were shown in Table 3.1.

Table 3.1 Vertical linear measurement results under different working RPM.

Rotation speed	H (mm)		D (mm)	
	Average	Deviation	Average	Deviation
90 RPM	3.03	0.14	0.67	0.08
360 RPM	2.84	0.14	0.83	0.08

We also measured the H and D value by digital caliper, which is 2.91 mm and 0.87 mm correspondingly. These results provide the ability to track the tool surface geometry characteristics. The deviation here indicates the difference of H and D along each black, red and blue line. The deviation resulted from the cutting tool geometry, although a few micrometer-scale deviations due to CCD camera pixel size could be involved. From the results, it is obvious that the deviation value remains the same for both 90 and 360 RPM condition, which represents the stable performance of the proposed technique. However, the different average value exits, and this comes from the quality of the "frozen image" under different working RPM.

3.5.3. Phase shifting mode

From the phase-locked mode results, when working RPM was 90, the surface reconstruction map showed the most complete results among other tests. Thus, the cutting tool was rotated under 90 RPM for the phase-shifting mode experiment, and the desired number of images per cycle was set to be 18 (20-degree imaging interval). A series of screenshots of the phase shifting 'frozen moment' is shown in Figure 3.9.

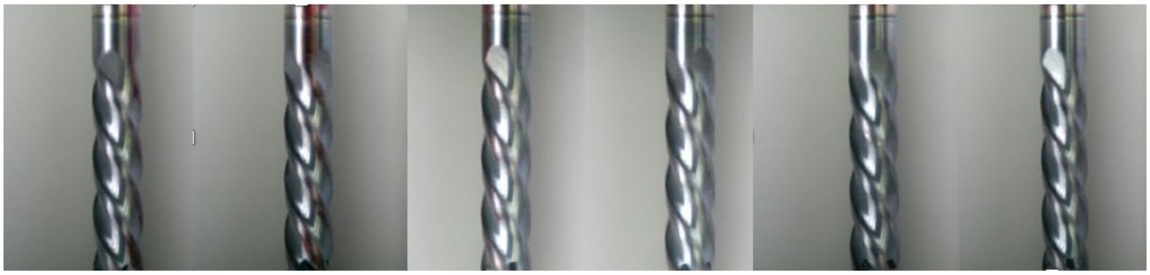

Figure 3.9. End mill tool phase-shifting raw image from location 1~6.

The center surface reconstruction is based on the stereoscopic algorithm. Before the depth map is recovered, pre-process for target centering, distortion removal, and brightness adjustment need to be done. Gaussian filter is applied to remove system noise. For the neighbor surfaces stitching process, SIFT (scale-invariant feature transform) [45] was used to determine the similar characteristics first, as they provided reference information. After the stitched panorama surface was generated, a whole surface phase unwrapping process was applied to remove the stitching errors. Figure 3.10 shows a stitched geometry expanded surface map and a vertical wave-fall map based on the phase-shifting process.

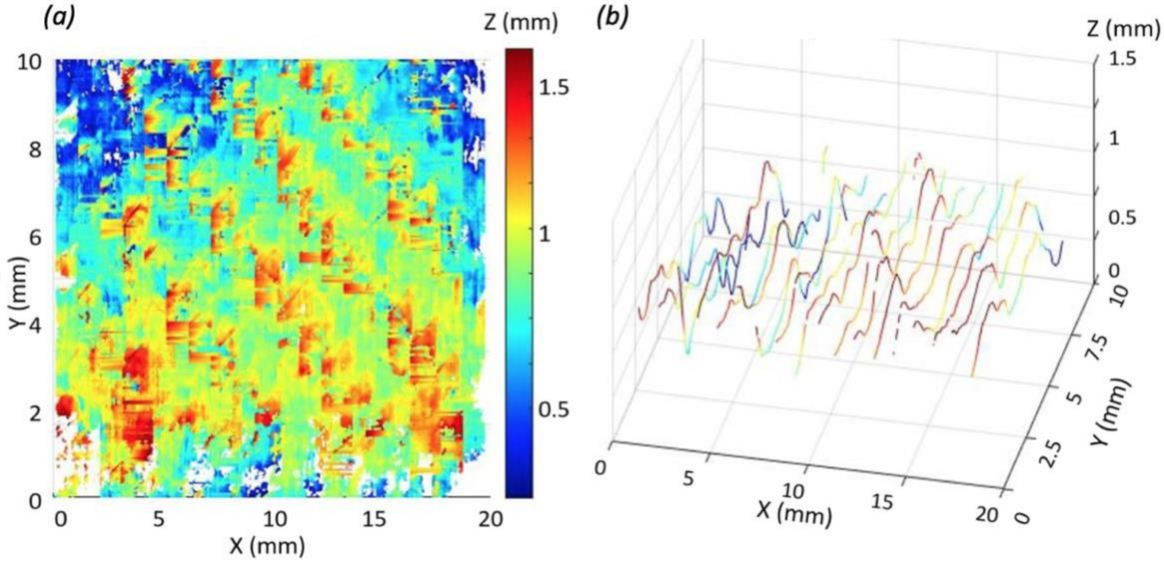

Figure 3.10. End mill tool phase-shifting geometry expanded panorama surface map (a) and the vertical wave-fall map (b).

The preliminary study experiment was performed on an end mill tool (ø1/8”), two working modes: phase-locked and phase-shifting modes were simultaneously operated. The phase-locked mode process showed the possibility of reconstructing the surface geometric information, such as surface roughness and shape, and tracking the surface characteristics, such as the grove depth and length. The phase-shifting mode showed the whole-view surface map reconstruction ability.

3.5.4. Rough surface target measurement

For further development on this technique, in addition to CCD with high frame rates, the laser scanning process for the structured light including spectroscopic approaches scan will be added to the system and will also be synchronized with spindle motion and illumination system, which can help collect tool edge conditions and dynamic performances. This combination of strobo-stereoscopy and laser scanning can improve the

3D image quality toward in-process characterization and identification of cutting tool dynamic behavior and cutting tool conditions.

Based on the geometry information reconstruction of the target end-mill tool, another potential of the proposed technique is the pattern recognition and construction for the roll-to-roll manufacturing industry. Here, a demonstration was performed on a dinosaurs-patterned wood rolling pin (ø 76mm, in Figure 3.11) with 30 RPM, together 18 images were taken for the whole view reconstruction.

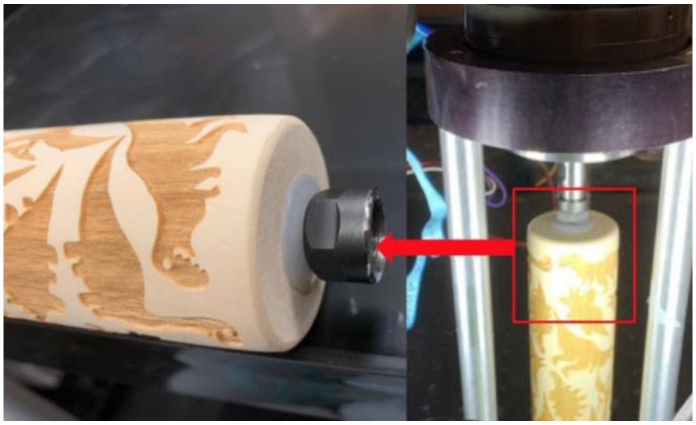

Figure 3.11. Dinosaurs-patterned wood rolling pin.

A series of screenshots of the phase shifting 'frozen moment' is shown in Figure 3.12.

Figure 3.12. End mill tool phase-shifting raw image from location 1~5

Under the same method, Figure 3.13 (a) showed a stitched geometry of the expanded surface map. Based on the target diameter and the calculated depth information from Figure 3.13 (a), Figure 3.13 (b) showed a reconstructed 3D rolling pin map, and Figure 3.13 (c) represented the top view of the 3D rolling pin map.

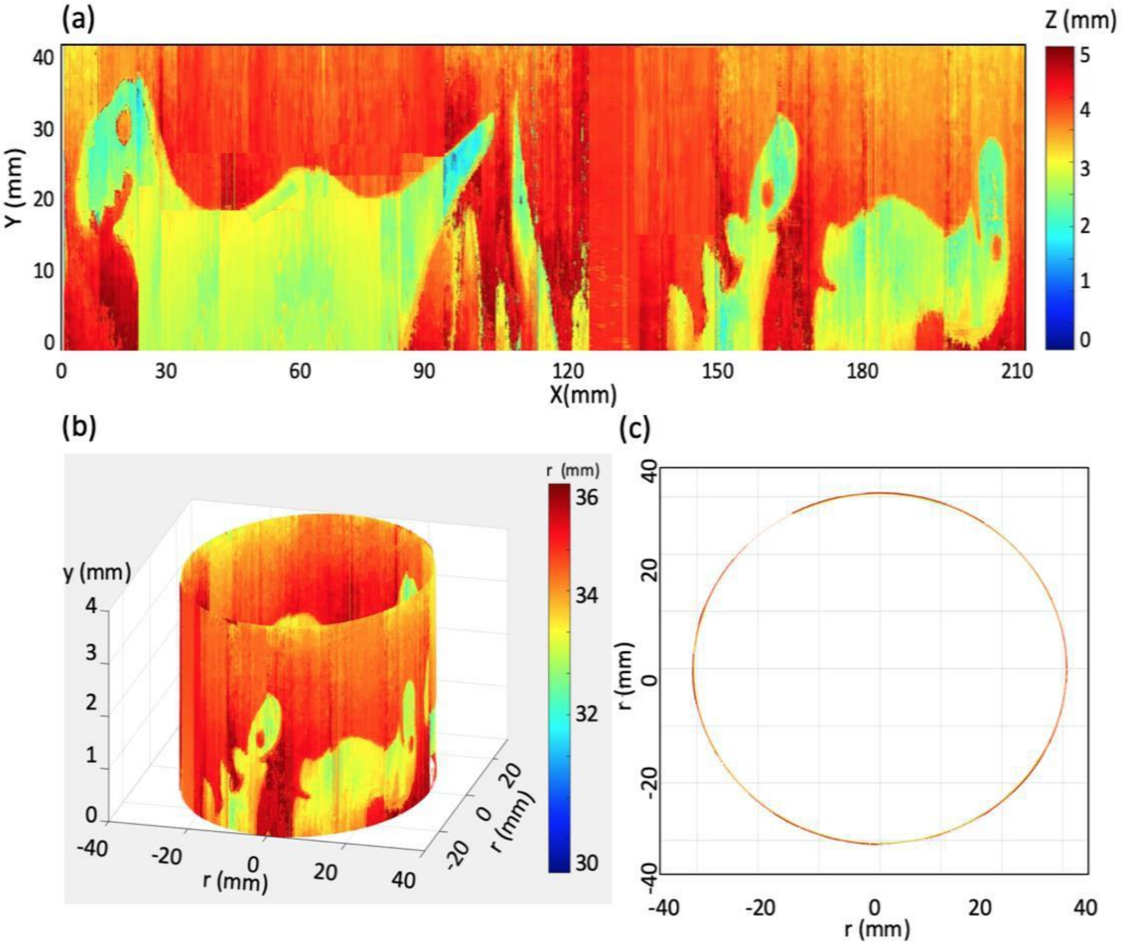

Figure 3.13. Dinosaurs-patterned rolling pin whole view reconstruction results, stitched geometry expanded surface map (a), the reconstructed 3D rolling pin map(b) and the top view map (c).

As a result, the proposed methods have potentials to offer more detailed and less noise information on the low-speed measurement and can clearly perform the pattern recognition and reconstruction process. Further study on image processing to remove data outliers will improve the image quality.

3.6. Conclusion

The principle of the phase-shifting strobo-stereoscopic 3D imaging process was first introduced and was preliminarily validated. The measurement system was developed, and the 3D reconstruction algorithms and phase-locked and -shifting algorithms were newly created. The spindle motion was successfully synchronized with strobo-light signals. The preliminary study results showed that the proposed strobo-stereoscopy could in-process measure the cutting tool geometry and reconstruct 3D images in the 360-degree whole-view that have the potential to monitor the tool conditions.

The proposed measurement method could be utilized for on-machine measurement in various manufacturing processes. The system performance can be significantly improved by using high-speed cameras with high frame rate and the light illumination system, and this measurement method combined with advanced image processing techniques can achieve less noise and more detailed surface reconstruction, which is able to perform the pattern recognition and reconstruction of various objects in 3D.

For the future work, the proposed 3D imaging technology will be further improved by combining strobo-stereoscopy and spectroscopy that can measure not only the 3D shapes but also 3D spectral properties of the rotating target objects. This advanced measurement method will enable to in-process monitor the conditions and status of the target object and the whole system’s dynamics.

4. FLUORESCENT STROBO-STEREOSCOPY[*]

This chapter demonstrates a fluorescent fluid implemented strobe-stereoscopy technique for high specular and non-distinct pattern surface inspection.

Sec 4.1 introduces the background of Fluorescent fluid and its common applications. Sec 4.2 compares the intermedia effects on high specular surface. FSS system setup and methodology is in Sec 4.3. Experiments and results are included in Sec. 4.4, where the ground and polished aluminum cylindrical are compared, using full-reversal method, cylindricity is calculated and compared with CMM results. An aluminum coated patterned surface is measured and successfully reconstructed.

4.1. Fluorescent Fluid

Fluorescent fluid has been implemented on monocular and binocular fluorescence microscopes for shape and deformation measurements at the microscale and even the nanoscale by tracking fluorescent particles[74]. This technique, however, has not been used with regular optical imaging systems at the macroscale so far.

For test objects without surface natural textures, speckle pattern fabrication is an essential and important procedure in machine vision measurements. The accuracy and precision also rely heavily on the quality (i.e., contrast and stability) of the decorated speckle patterns[75].

Benefitting from the small size and biocompatibility of fluorescent particles, the

---

[*] Reprinted with permission from “Fluorescence strobo-stereoscopy for specular reflection-suppressed full field of view imaging” by Xiangyu Guo, ChaBum Lee, 2022, Measurement,Vol.192, 110907, © 2022 Elsevier Ltd. All rights reserved.

fluorescent dye is introduced to the system long with another two characteristics. One is the Stokes shift, which occurs when the dye is activated by a certain ultraviolet (UV) light.

Its emission wavelength is shifted and does not overlap with the exciting wavelength. Assist with the band-pass filter, specular reflection from the exciting wavelength can be separated. Another advantage is the ability to increase speckle contrast, which helps improve reconstruction accuracy for the presence of more reference matching points in the pair of images.

It is widely recognized that the quality and appropriateness of lighting are critical components of developing high-quality, robust, and timely vision inspection for stereoscopy systems. Due to the directionality of the surface specular reflection, the quality of 3D surface imaging can be significantly reduced, and the surface information beneath the specular reflection area can be lost. The more refined the machined surface, the more critical specular reflection becomes.

A fluorescent fluid or dye may be used to eliminate specular reflection from the machined shiny surface. Stokes Shift explains one of the fluorescent dye's properties, namely that the dye's emission wavelength is shifted when excited by a specific ultraviolet (UV) light. As a result, the specular reflection can be distinguished from the stimulating wavelength. Meanwhile, the fluorescent liquid is well-known for enhancing speckle contrast and enabling simultaneous observation of multiple surface textures. The geometry, shape, area, and depth of the target sample can be used to characterize and analyze the defects as well as the tool wear situation beneath them.

4.2. Fluid Intermedia Effect

In order to test the effectiveness of the FSS, the fluid effect is discussed first. The three different mediums (air, water, lubricant liquid) were applied to the polished cylinder. The reconstructed images in the framed area are shown in Figure 4.1. It appears that a higher viscosity fluid on the surface can reduce the specular effect.

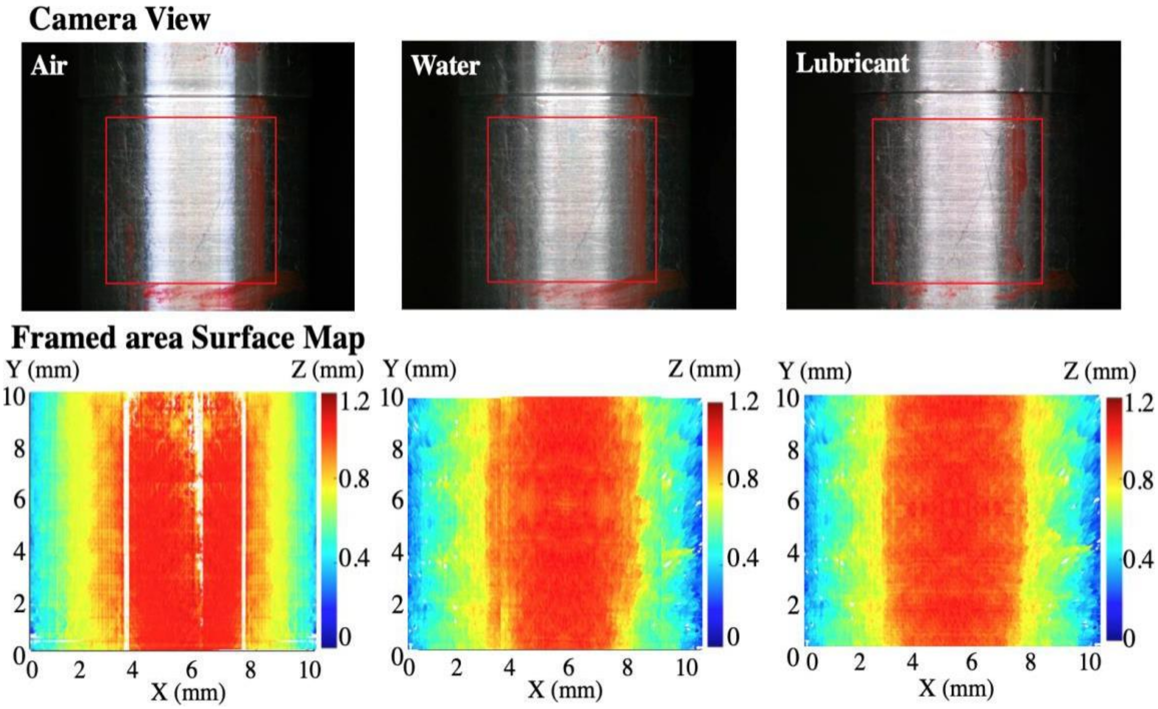

Figure 4.1. Fluid media effects on the cylindrical surface.

According to the results above, the liquid-applied casings can collect information about the blank area caused by the specular effect. In comparison to the other two situations, the lubricant liquid-coated surface diffuses the most specular light. This is illustrated by the findings of the framed area surface map, which shows that the lubricant-liquid-coated surface is capable of reconstructing the complete surface map while being least affected by specular light. The water condition of the framed area surface map is not lacking information; yet, the non-continuous strokes along the specular light area demonstrate that such a rebuilt surface is impacted by the light distribution. The results indicated that the general liquid can assist reduce the specular effect, and that liquids with a higher viscosity result in a smoother surface quality.

In the camera view of Figure 4.1, the tool mark, however, is the least clear in the lubricant case and less clear in the water case compared with the air case. This can also be proved by the surface map, as fewer structures exist in the media-introduced case. Thus, the scattering effect from the general liquid helps reduce the directional reflection intensity. The viscosity value is critical as it affects the quality of the surface reconstruction. However, such liquids can result in a blur or even a halo on the surface as it reduces the contrast at the same time. As a result, we proposed applying the fluorescent media to directly remove the specular effect without introducing irrelevant environmental noises. Fluorescent liquid absorbs the incident wavelength and converts it to another. By employing a bandpass filter, it is possible to minimize directional reflections while maintaining or even increasing the target area contrast.

4.3. Fluorescent Strobo-Stereoscopy Methodology

Stereoscopy is a 3D imaging technique for adding the illusion of image depth to two surface images captured by a pair of vision camera units, and measures shape, displacement, deformation of the measurement target surfaces [76-80]. The measurement accuracy and precision of stereoscopy are determined by the performance of vision cameras such as pixel size, focusing lenses, frame rate, and so on. However, stereoscopy is limited to the highly reflective surface measurement where specular reflection exists on the smooth surface known as glare, which causes a lack of information on the directional reflection area and reduces the brightness and contrast of the rest of the scanning area[80,81]. So, strong specular reflection in the imaging systems causes strong highlights in the imaging devices and results in surface information loss. Figure 4.2 presents the example on the reflection effects on target distinction under camera view.

Figure 4.2. reflection effect on plastic wrapped barcode target[82].

Many pieces of researches have been conducted to characterize and remove specular reflection problems using color, polarization, multiple views, and multi-flashing [83-85]. Those methods are primarily focused on imaging systems and display devices such as lenses, back-light units, glasses, or optical films. Recently, efforts to increase the measurement resolution and enhance imaging quality through scattering media such as fluorescence dye-doped fluids were introduced [86-89]. However, those methods are limited to stationary target surface measurements or slow dynamic motion and deformation measurements.

The fluorescent dye has two intrinsic characteristics. One is the Stokes shift, which occurs when the dye is activated by a certain ultraviolet (UV) light. Its emission wavelength is shifted and does not overlap with the excitation wavelength. When the fluorescent liquid is applied to the surface, its emitted direction is random. Thus, along with the band-pass filter, specular reflection from the excitation wavelength can be separated. The other advantage is the ability to increase speckle contrast, which helps improve reconstruction accuracy for the presence of more reference matching points in the pair of images.

Prior to the measurement, the fluorescent fluid was chosen as the mixture of Pylakrome LX-10215 particles (from Pylam Company) and fluorescent fluid PAG 150 oil. The excitation wavelength of the light-emitting diode (LED) light source was chosen as 365 nm and the emission wavelength measured by the spectrometer was 520 nm (central peak value) as seen in Figure 4.3.

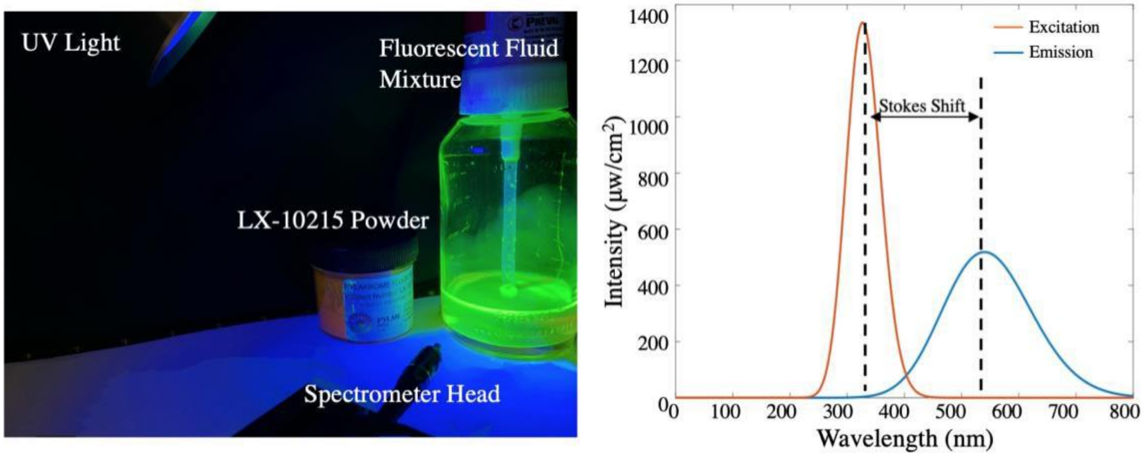

Figure 4.3. Fluorescent-reflective fluid fabrication (left) and stokes shift effect (right).

The experiment setting and the proposed FSS method were depicted in Figure 4.4 (a). A pair of charge-coupled device (CCD) cameras were employed for the image capturing, a 365 nm ($\lambda_{excitation}$) UV light was prepared for the excitation light source, a pair of high-pass filters (BPF >370 nm) were chosen from the emission wavelength 520 nm ($\lambda_{emission}$) of the fluorescent fluid, and a rotary spindle was used for the target rotation. Using the fluorescent fluid can remove the sensitivity of the illumination system while highlighting the contrast, hence increasing the number of reference points, and the fluorescent fluid is sprayed to the surface in a spray bottle while the target sample is rotating.

To show the advantage of the fluorescent fluid in eliminating specular reflections, a comparative result of reconstructing a 3D surface with the machined aluminum rod (ø1") is shown in Figure 4.4(b), showing that the fluorescent liquid can improve the optical quality-surface map reconstruction ability.

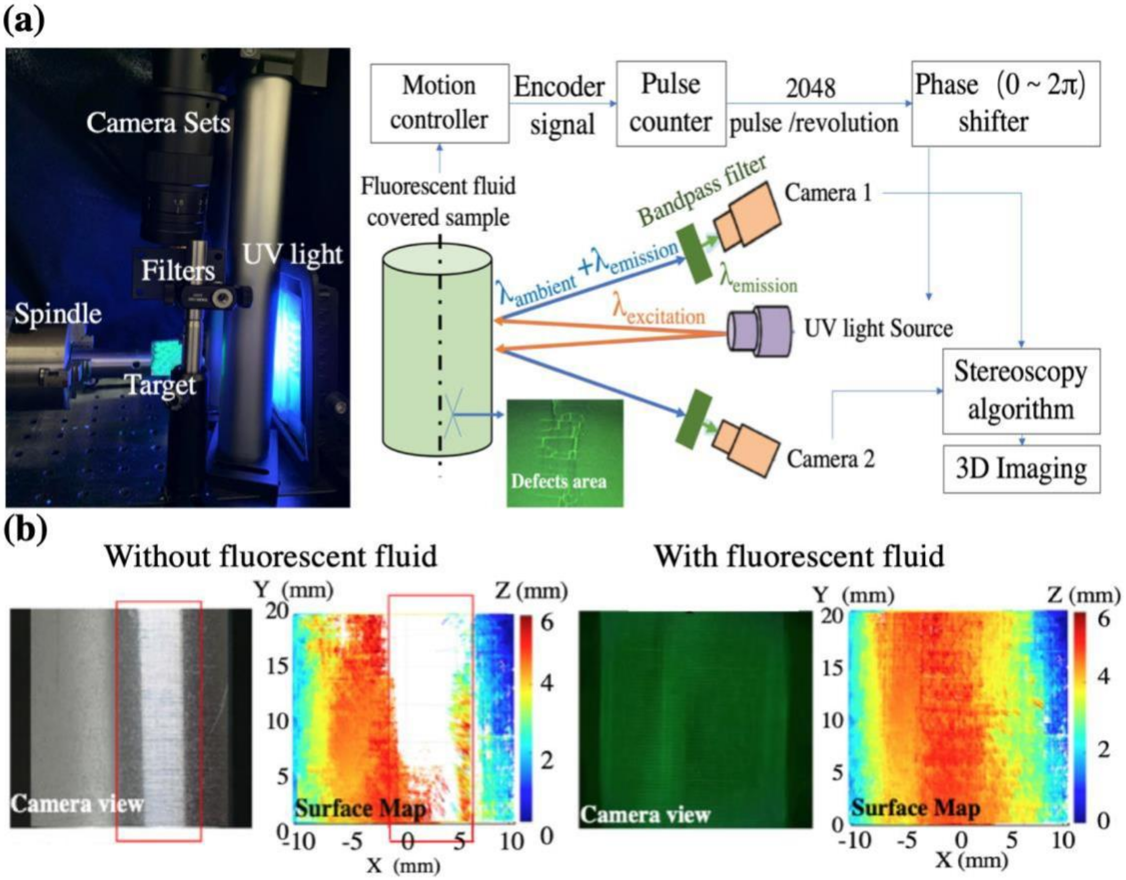

Figure 4.4. Principle of fluorescence strobo-stereoscopy: (a) experiment set-up and schematic diagram (b) single image reconstruction comparison on an ø1" rod under with and without fluorescent fluid conditions.

4.4. Experiment Results

Comparison experiments on the targets with a rough surface and a polished surface were conducted between normal LED conditions and UV light conditions with fluorescent fluid. These results prove that the fluorescent fluid is capable of reconstructing the specular effect that existed on the surface. After this, the patterned structure target was measured to first track the FSS single image reconstruction ability on the pattern recognition, second to demonstrate the whole view reconstruction process. Finally, the cylindricity and roundness on the reconstructed 3D target were compared with the baseline data obtained by using the coordinate measuring machine (CMM) at Zeiss. All the samples are cylinder structures (ø1").

4.4.1. Surface quality effects under FSS methods comparison

Rough surface quality and the polished surface on the Al cylinder quality are compared in this session. Figure 4.5 presents the surface reconstruction results on the red-framed area. The center line extraction along the vertical direction is also presented in Figure 20, the tendency on the linear results are similar. Based on the ASME B46.1-2019[90], arithmetic average Ra value, can be calculated by the absolute values of the profile height deviations from the mean line is also calculated.

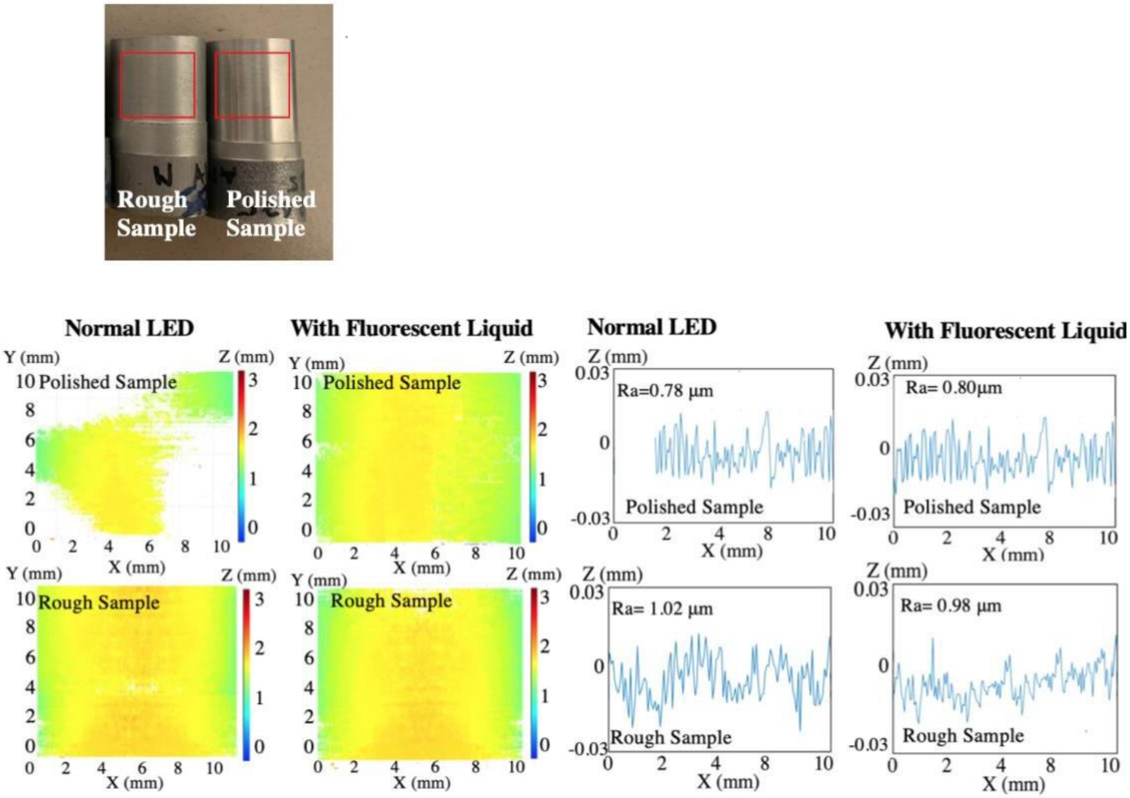

Figure 4.5. Imaging results of the normal LED and UV light with fluorescent liquid for rough and polished surface comparison.

The Ra values measured on the normal LED and the fluorescent liquid cases for the polished surface case are 0.78 μm and 0.8 μm, respectively, and the direct difference ratio is 2.6%. Even though this difference is slight, the reconstruction ability under the normal LED case is limited due to the blank section. This is because of the specular light effect. For the rough surface, the measured results are 1.02 μm and 0.98 μm for the normal LED and the fluorescent liquid case, respectively, with the variation of 3.9% variation. Even if the variations are all within 5%, it is difficult for the normal LED condition to perform the complete single image reconstruction.

The 5 by 5mm single surface area reconstruction was compared with the Alicona confocal microscopy on a 1’’ reference cylinder. The results are shown in Figure 4.6. Horizontal linear scan was extracted for the radius of curvature comparison. The vertical linear scan was also compared with the contact profilometer, which was presented in Figure 4.7.

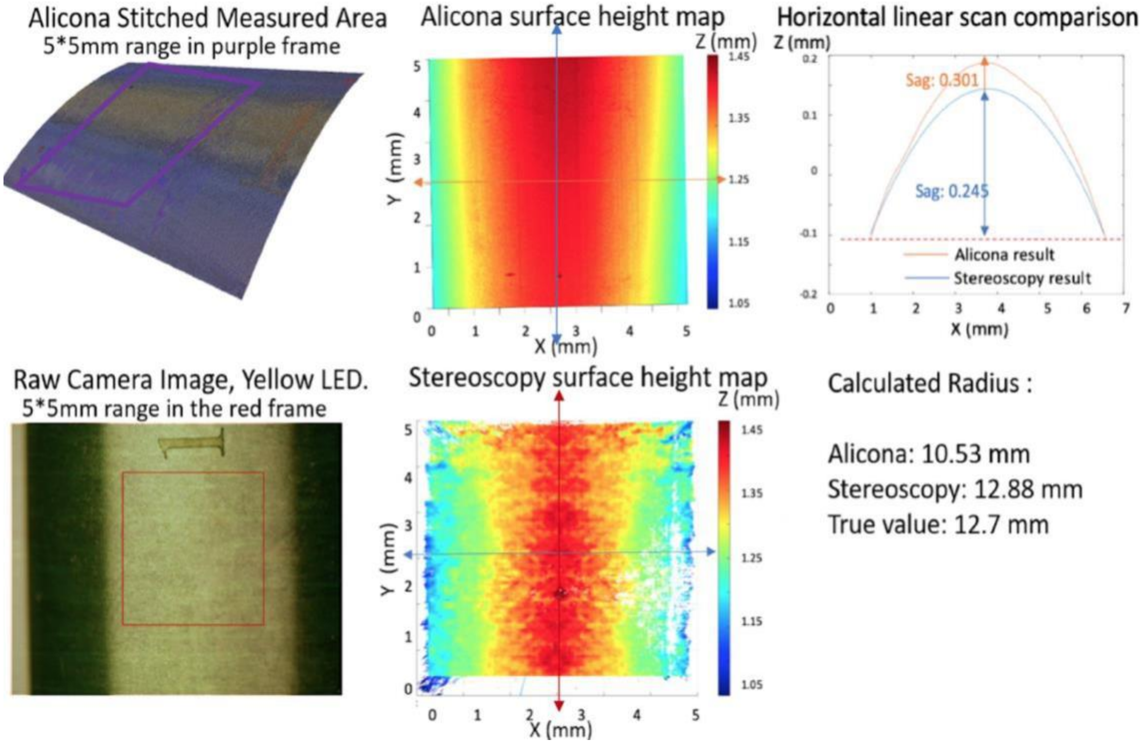

Figure 4.6. 1’’ Dia. rod surface reconstruction comparison among stereoscopic, Alicona confocal microscope in the surface map and the horizontal scan.

The similar distribution was observed from the reconstructed surface results. The stitching process was required for the confocal microscopy technique, thus from the horizontal scan results, the calculated radius of curvature value varied from the reference results 10 times than the stereoscopic method.

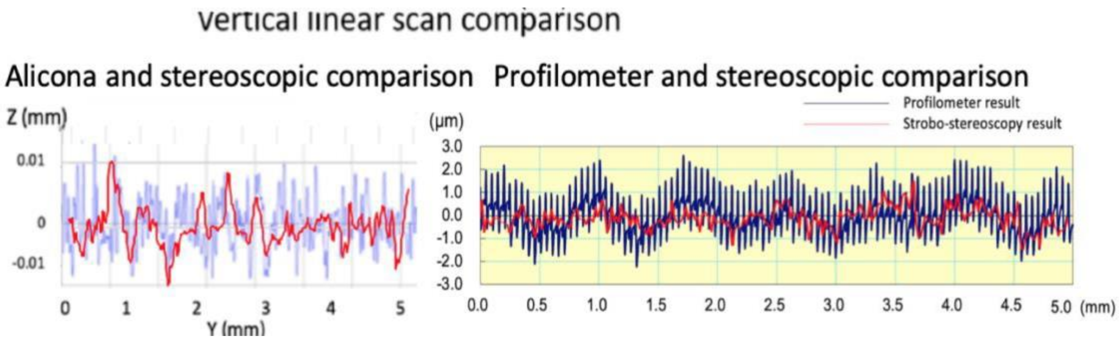

Figure 4.7. 1'' Dia. rod surface reconstruction vertical linear scan results comparison among stereoscopic, Alicona confocal microscope and profilometer results.

The stereoscopy method also shows a good agreement on the mid-frequency distribution on the vertical linear scan results for both confocal microscopy as well as the contact profilometer results.

4.4.2. FSS on patterned surface

To show the advantage of the use of the fluorescent fluid in eliminating specular reflections and to analyze the performance, a comparison of with and without fluorescent liquid applied surface reconstruction was completed and compared, as is shown in Figure 4.8. and Figure 4.9. A flat surface with an aluminum-coated square-patterned structure was selected as a reference target. Though the peak-valley information can be picked up by the reconstructed map, the detected square-patterns are distorted because of the directional specular effect.

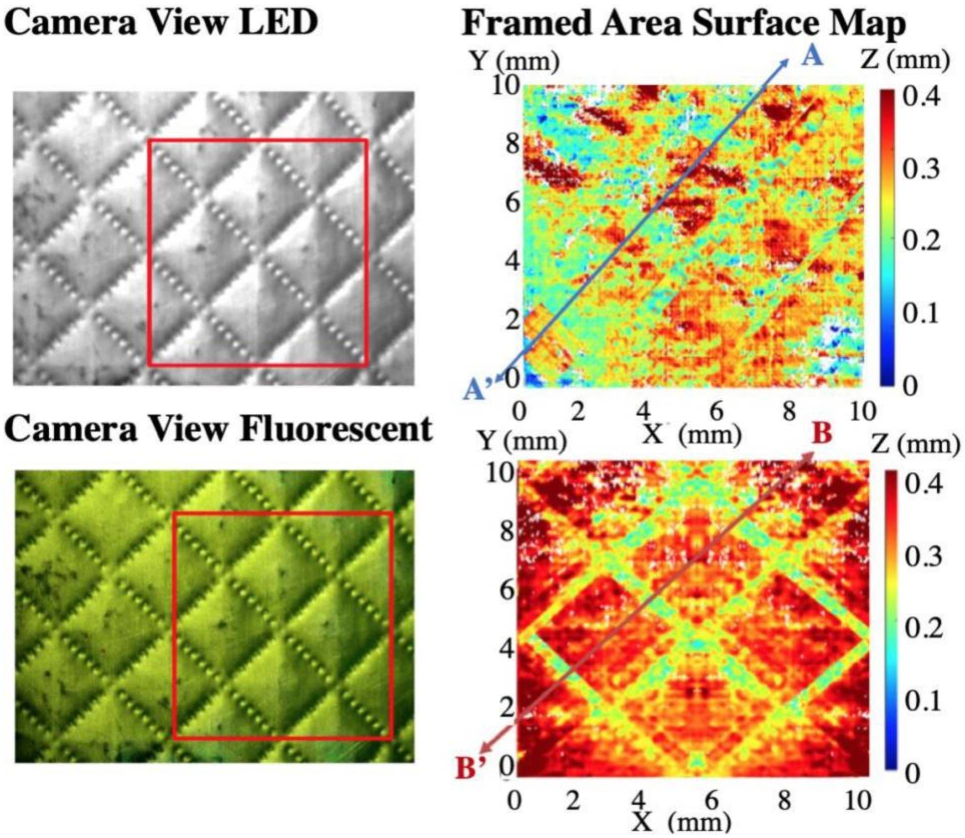

Figure 4.8. Comparison of SS and FSS imaging surface map results.

A comparative experiment with commercial metrology instruments was conducted to assess the surface reconstruction performance. To confirm the accuracy of the linear scan from the reconstructed surface by the FSS method, a digital microscope, and laser displacement sensor (LDS, Keyence LK-G35) 1D measurements along the pattern direction were chosen, which are also shown in Figure 4.9.

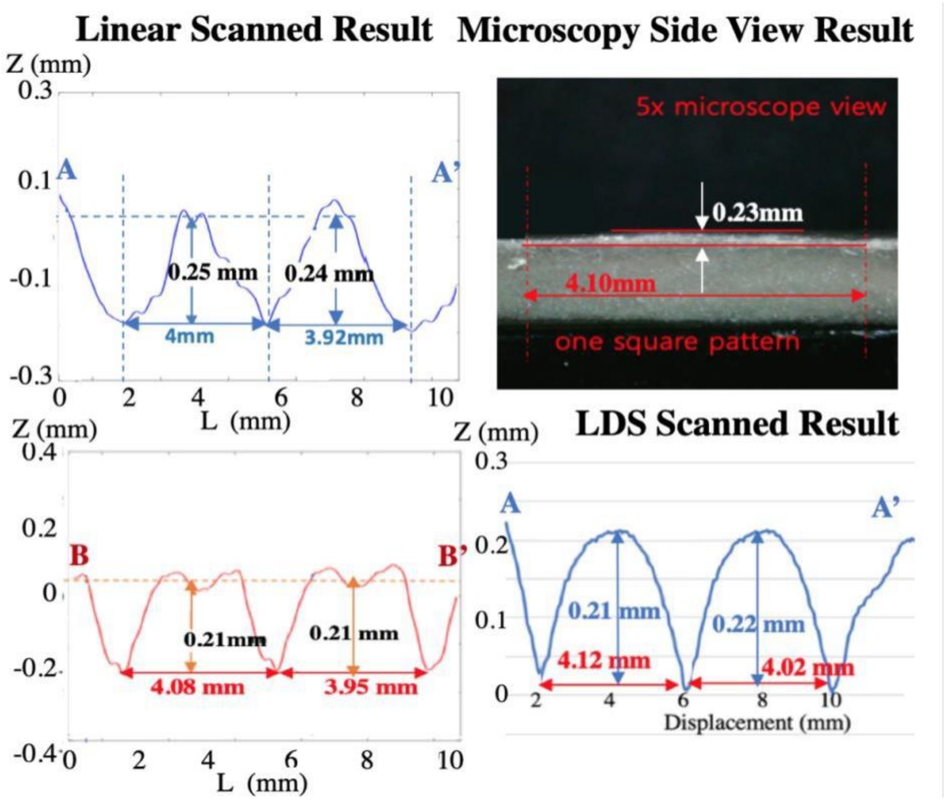

Figure 4.9. Comparison of SS and FSS imaging linear scan results.

From the results shown above, it can be seen that fluorescent liquid-applied cases can present the pattern clearly. Table 4.1 compares the average measurement results of two pattern squares in the linear scanned results obtained by the LDS, conventional SS and FSS .

Table 4.1. Linear scanned comparison results.

	LDS	**FSS (with fluorescent fluid)**	**SS (without fluorescent fluid)**
Length (mm)	4.070	4.015	3.96
Depth (mm)	0.215	0.21	0.245

The LDS results are applied as references, and the FSS measured values are more similar. The absolute differences in length are 0.055 mm and 0.11 mm for FSS and SS, respectively, and the difference ratios are 1.4% and 8.1% for each case. Similarly, for the depth situation, the absolute differences are 0.005 mm and 0.03 mm, with 2.3% and 13.9% difference ratios, respectively. The FSS method results are closer to the reference results, and compared with the SS method, it improves 6.7% in the lateral direction and 11.6% in the axial direction.

Furthermore, to prove the capabilities of full cycle 360° 3D target reconstruction, the experiment is performed on an ø2" rod with the same patterned structure. The target was fixed on the spindle with a 30 RPM rotating speed. Together, 16 images were taken per cycle (360°) for the stitching process, which means that the pair of cameras captured images when the spindle rotates every 22.5°. The whole view reconstruction process, along with the FFOV, is in Figure 4.10.

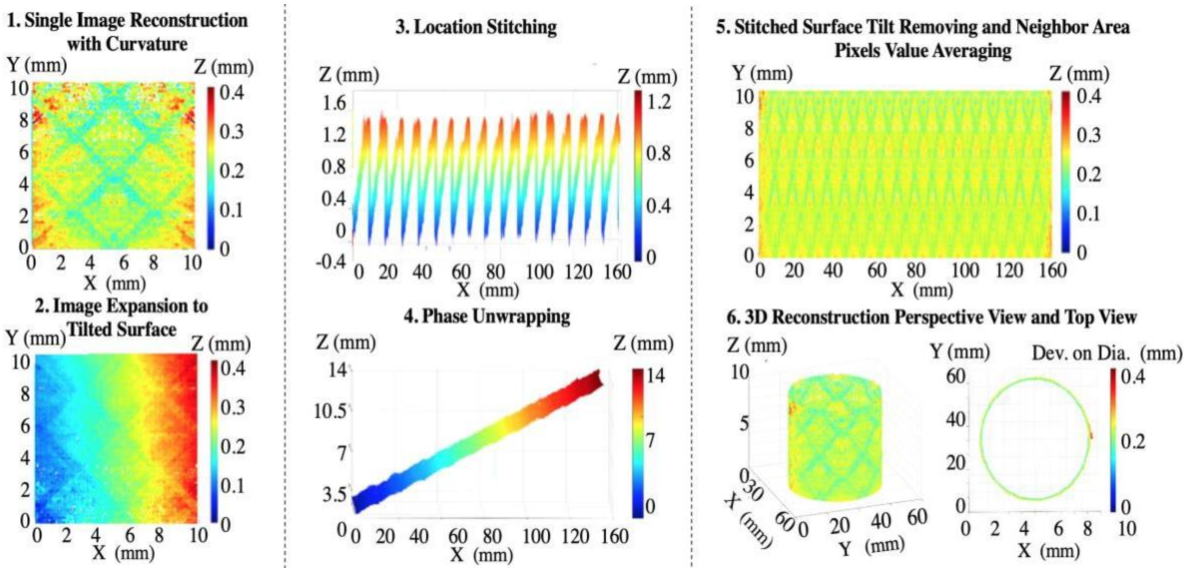

Figure 4.10. A full field of 3D FSS image reconstruction process of a target rotating at 30 rpm.

The stereoscopic algorithm was first used for single image reconstruction. For convenient neighbor image location stitching, the original curved images were expanded to the tilted images. With the known rotation angle, a phase unwrapping process was applied to generate a tilted stitching map. The panorama surface is gathered following the balancing process, and the 3D full view can eventually be reconstructed. This validates the ability to reconstruct the whole 3D view for cylinder-based targets.

4.4.3. Dimensional errors inspection

As the whole view reconstruction is achievable, the cylindricity and the roundness error can be analyzed. The FSS process was performed on a reference gauge pin. The results were compared with the CMM measurement analyzed by Zeiss. Together, 5 layers along the z axis were measured to test the cylindricity, which was 1.788 μm, and each layer's diameter level were also gathered for roundness calculation, which showed that the average deviation was 1.788 µm ±0.090µm. Figure 4.11. shows the FSS whole view reconstructed results, along with the extracted 5 layers top view results. The variation on the cylindricity 2.5 µm and the roundness error 2.12 µm ±0.166µm. The CMM and FSS results showed good agreement in terms of the cylindricity and roundness error.

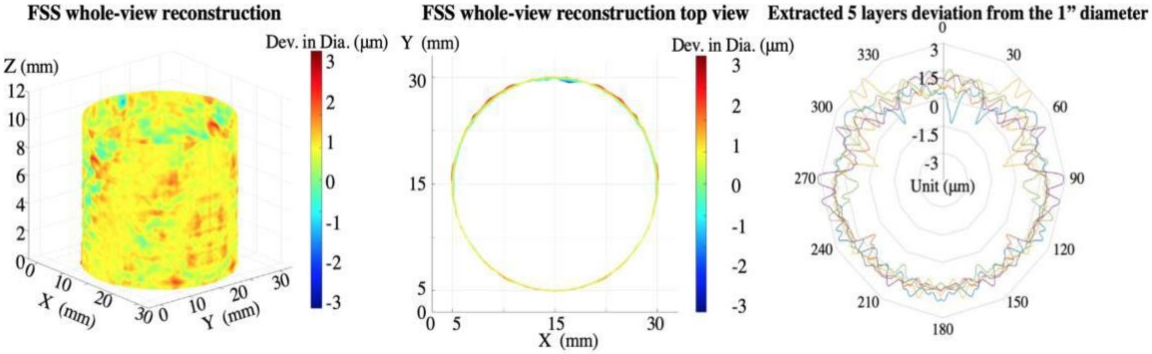

Figure 4.11. A full field of 3D FSS image.

The SS examined results under same condition are presented in Figure 4.12. Compared with the FSS results, the distribution on the peak and valley are similar, but high noise level existed, this is because of larger number of images to complete a whole cycle, and the reflection noises. Table 4.2. summarized the measured cylindricity, diameter variation for all methods, which are Zeiss CMM, SS and FSS method.

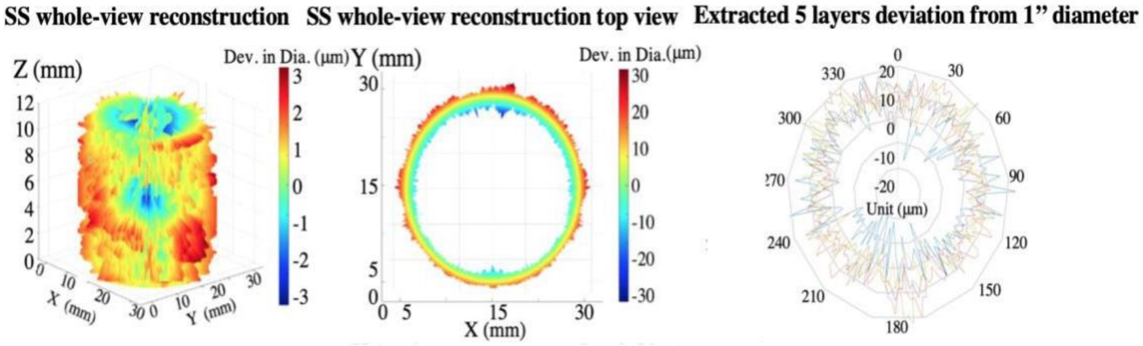

Figure 4.12. A full field of 3D SS image.

Table 4.2. Linear Zeiss CMM, SS and FSS measured results comparison

Method	Cylindricity	Diameter Variation
Zeiss CMM	1.788 µm	1.788 ± 0.090µm
SS	13.81µm	20.9 ± 3.56µm
FSS	2.5 µm	2.12 ± 0.166µm

The noise level under the FSS method reduced 10 times than the SS methd, and more similar to the reference CMM measured results, which prove the ability to reduce the reflection light noise level and image stitching level.

4.5. Conclusion

This chapter introduced the FSS method to solve solid specular reflection, which causes the false reconstruction on the highly reflective surface and provides on-machine FFOV 3D reconstruction of the rotating part. The FSS method, as well as the principle of fluorescent liquid implementation, was demonstrated and validated. The comparison experiment of different fluid media demonstrates that higher viscosity liquid giving better response on the specular reflection. The comparison of the surface quality samples reconstruction proves that the FSS performs stronger in the polished surface.

Based on the aluminum-coated square-patterned surface, a demonstration was finished by comparing the flat surface reconstruction with and without fluorescent liquid. For a baseline comparison, commercial metrology instruments the laser displacement sensor and the microscope were applied to compare the variation on axial and lateral direction, where those values of FSS were 2.3% and 1.4%, respectively, while for those results in the standard white light LED case were 8.1% and 13.9%. This proves the benefit from the fluorescent fluid implemented system.

A full view reconstruction of such patterns on the cylinder structure was completed. Meanwhile, a validation process was performed with the Zeiss CMM measurement on 1" gage pin. The cylindricity and the diameter deviation is compared. As the fluorescent dye is immersed in the cutting fluid, this technology can be employed as an on-machine or even in-process metrology for ongoing development, regardless of the on-machine goal measurement setting.

5. IMAGE SEGMENTATION AND EXTRACTION POST-PROCESSING TECHNIQUE*

This chapter presents a feature-selective segmentation and merging technique to achieve spatially resolved surface profiles of the parts by 3D stereoscopy and strobo-stereoscopy. Conventional filtering processes of the 3D images involve data loss and lower the spatial resolution of the image.

Sec 5.1 introduces the overview of 3D surface image segmentation techniques. Sec 5.2 presents this proposed post-processing technique principle. Sec 5.3 shows experimental results which were compared with those of conventional filtering methods by using Gaussian filters and bandpass filters in terms of spatial frequency and profile accuracy. Conclusion is in Sec. 5.4.

5.1. Image Segmentation Techniques Overview

5.1.1. 3D imaging process applied fields

3D imaging process is to create the depth map in an image by manipulating 2D image data into 3D image data. In many industrial applications, 3D imaging techniques aid to identify the structures and patterns. Since 1832, when English physicist Sir Charles Wheatstone invented stereoscopy, several investigations on 3D imaging techniques such as interferometry, stereoscopy, time of flight (TOF), and structured light scanning have

---

* Reprinted with permission from "Spatially resolved stereoscopic surface profiling by using a feature-selective segmentation and merging technique" by ChaBum Lee, Xiangyu Guo, 2022, Surface Topography: Metrology and Properties ,Vol.10, 014002, © 2022 IOP Publishing Ltd. All rights reserved.

been performed [91]. While interferometry is typically used to scan smooth surfaces at a fraction of a wavelength [92], other techniques, such as single or dual cameras, are also available to provide millimeter-micrometer-resolution surface geometry [93]. Sheppard invented confocal scanning optical microscopy [94]. Guo estimated the geometry of rotating parts using stereoscopy and stroboscopy [95]. Kassamakov demonstrated a three-dimensional imaging approach based on Mirau interferometry for scanning grooved surfaces [96]. To generate super-resolution stereoscopic images, Song devised an approach for assuring stereo consistency across stereo image pairings [97]. Yan demonstrated how to adjust the disparity range of stereoscopic image pairings, so resolving the disocclusion problem [95]. Compared to interferometry and microscopy, the stereoscopy technique is widely utilized in the industry because of its simple structure composition and resistance to environmental influences.

The industry desires high-precision and accurate image reconstruction and fully automated part measurement and inspection. Denoising, contract enhancement techniques, and machine learning algorithms that produce high-quality images while maintaining imaging features are critical for image standardization and generalization in a wide variety of industrial applications [98-102]. For inspecting measurement samples, 3D machine vision-based imaging techniques for 3D surface profiling, reconstruction, and feature definition have been widely reported published. By increasing the picture sampling and spatial resolution of high-frequency signals via computer vision techniques, super-resolution imaging approaches based on deep learning algorithms improve image quality [99, 103-105]. These techniques produce more lifelike and can be used for a variety of high-resolution microscopy applications. However, because of the complexity of the technique, creating super-resolution photos from a collection of low-resolution images demands considerable computational effort and expense [102].

Along with advancements in 3D imaging technologies and image synthesis, numerous researches have shown the potential for machine learning or artificial intelligence algorithms to improve image quality significantly. The super-resolution imaging technology overcomes the spatial limits of optical imaging systems by mixing low-resolution noisy blurring images with the high-resolution image. By adaptively estimating the point spread function, Yoo built an ideal super-resolution image network [106]. Dong trained a deep learning algorithm to map low- and high-resolution images [107]. To achieve high spatial resolution images, multiple machine learning or artificial intelligence-based technologies were applied. Because super-resolution imaging techniques are computationally prohibitively expensive for large-scale imaging [107-108], they have been mainly used to imaging a small area or volume, with a particular focus on microscopy [108].

5.1.2. Requirements for implemented 3D image processing

The 3D vision system must be fast, robust, small, and economical to get target measurements in macro-scale for online measurement. In this article, raw 3D images of a few tens of millimeter-sized samples were segmented based on their features adaptively. Rather than enhancing the full image at once, the quality of each segmented image was improved by using a super-resolution method to minimize computational complexity. As a result, the segmented images were reconstructed.

This proposed technique for selective feature segmentation and merging combines automated feature classification, feature-based adaptive image segmentation, and image reconstruction can achieve high accuracy, precision, and spatial resolution in 3D surface profiling while retaining imaging features.

We propose the image segmentation-based imaging post processing technique, in which an original standard digital camera image will be implemented to stereo reconstructed depth map. The initial generated depth map which, although is metrically accurate, to remove the environment effects such as the shadow effect, the distance and the tip or tilt angles from the camera to the target surface, target balancing and noise reduction processes are required.

While the 3D recognition is commonly applied on the medical imaging processing [109-110] and remote sensing field [111-112], the proposed technique is aimed at online manufacturing inspection. Based on the 3D reconstruction from the stereoscopy system, the implemented selective feature segmentation and merging can effectively recognize the desired structures or patterns. This technique can be applied for the roll-to-roll, molded inspection. Further with the development of micro-stereoscopic technique, and random feature classification, it can be applied for surface defects inspection on freeform based structure.

5.2. Image Segmentation and Extraction Principle

The Image segmentation and Extraction (ISE) is basically based on the feature separation technique to apply the filters for 3D image quality enhancement adaptively.

Filtering technology is a natural way to extract surface information, as well as multi-scalar features of 3-D surface [113]. Low frequency presents spaced irregularity on the sampled surfaces, or the profile information surface profile, while the high frequency presents the roughness and irrelevant form noise caused by the environment. Thus, a low-pass filter can be applied to generate the fitted surface map and a high-pass filter is capable of removing the roughness or the environmental noise information.

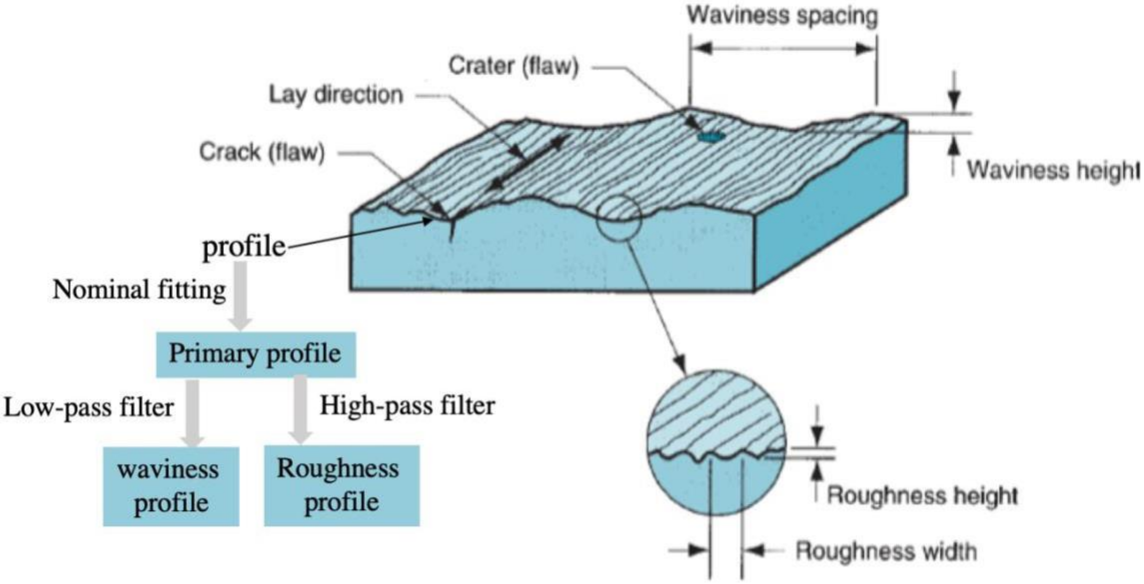

Figure 5.1.Surface profile, waviness, roughness components based on frequency distribution [114].

The definition to low-pass filter is defined below, where $\boldsymbol{H(u,\ v)}$ is a filter function, $\boldsymbol{\omega_0}$ is a cutoff frequency, (u,v) is a point on the frequency domain. The high-pass filter is defined in the opposite way. The filtering process can be implemented via Fourier transform[51].

$$H(u,v) = \begin{cases} 1 & if\sqrt{u^2+v^2} \le \omega_0 \\ 0, & otherwise \end{cases} \tag{12}$$

In this study, stereoscopy was employed for 3D imaging, and the ISE method was tested on the stereoscopic system. The Stereo Camera Calibrator app in MATLAB was used for the calibration [100]. Twenty images of the calibration checkerboard pattern at different orientations regarding the cameras were captured by the stereoscope system. The detailed checkerboard imaging process was explained in Section 3.1. Figure 5.2 is the flow chart of the ISE method towards the 3D reconstructed surface map.

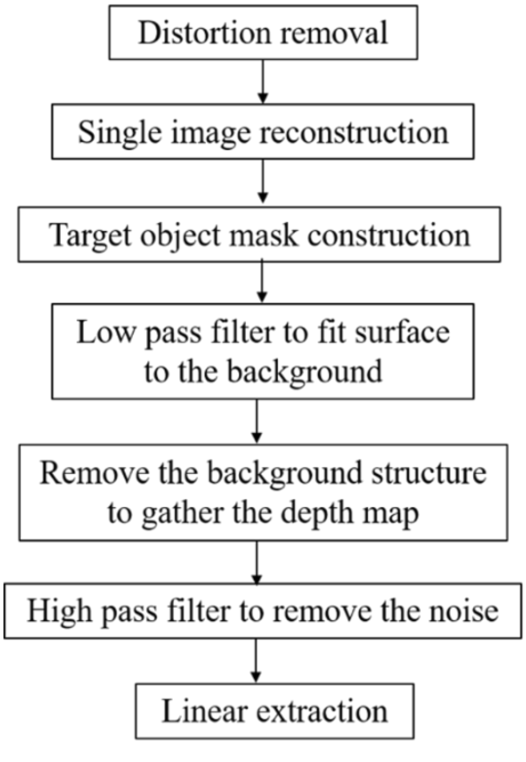

Figure 5.2. ISE process flow chart.

Together, ISE method is achieved by the following steps, and an example on a 3mm depth, 12.7mm dia. rivet is shown in Figure 5.3.

(1) lens aberration was removed to eliminate the image distortion.

(2) 3D reconstructed surface map is made by the stereoscopic technique with the aberration-removed image pair.

(3) the image was separated based on the features so that the background image and target image could be independently processed.

(4) low-pass filter was applied first for the background and target image surface fitting.

(5) two featured images were merged back to get the 3D image, and high-pass filter was applied for the noise deduction.

(6) the 3D image and profile were achieved by linear extraction.

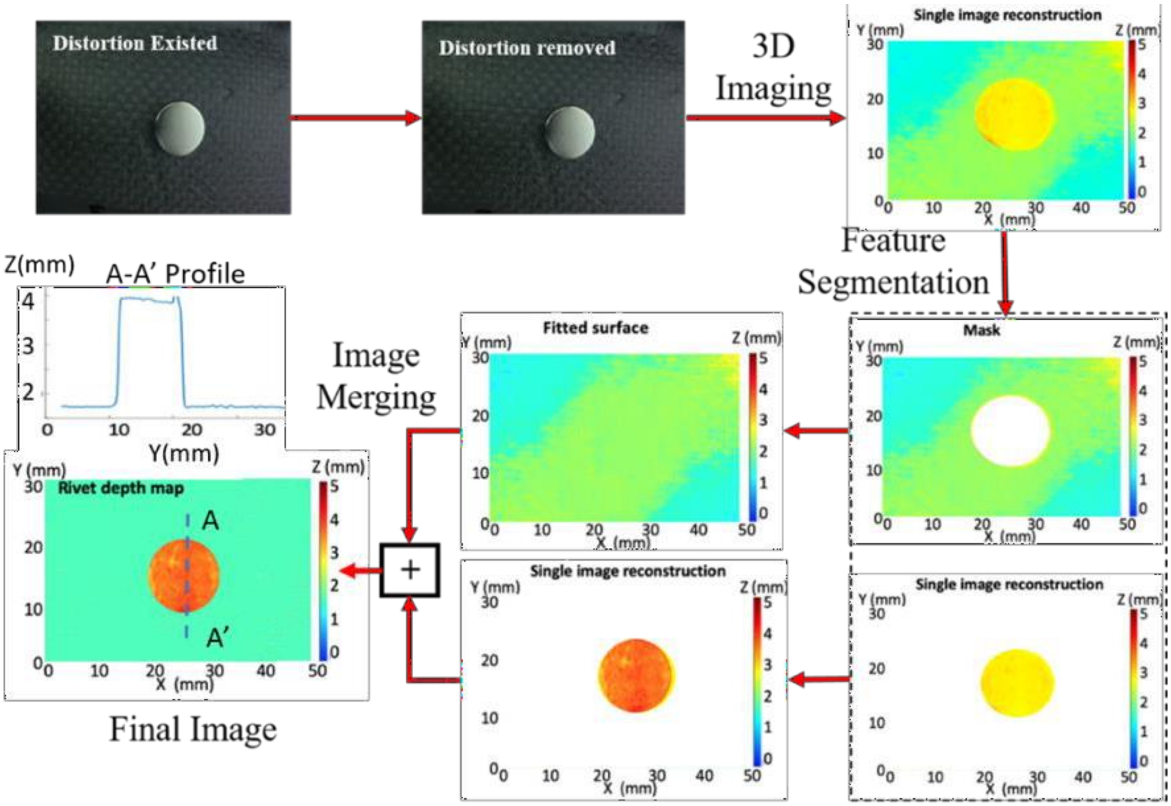

Figure 5.3. Feature-selective segmentation and merging: flow chart (left) and preliminary experiment results (right).

5.3. Experiments and Results

5.3.1. Stereoscopy based on ISE method

The stereoscopic technique is embedded with a pair of vision cameras capturing images of the measurement target. By applying the triangulation, lens equation, and aberration elimination method, the 3D image, the so-called depth map, is reconstructed by the location information of the same object points from both the left and right images. Figure 5.4 shows the principle of the stereoscopic imaging process. Camera 1 and 2 have their coordinate system on the charge-coupled device (CCD) frame. Here, f is the focal length of the lens, and B is the distance between two cameras. The image depth information D from the point P on the target to the CCD of the camera system can be calculated by [115],

$$D = f\,\left(\frac{B}{y_2 - y_1} - 1\right) \tag{13}$$

A stereo camera calibration is performed to determine the intrinsic and extrinsic camera parameters or the projection matrix coefficients of the system [88]. These parameters transfer the scene points in 3D space to their corresponding image points, thus the measured depth can be recovered. In this study, calibration was performed with the same camera systems for the target sample measurement. The measurement target was fabricated by attaching metal stickers with different thickness (t) with 0.1, 0.3, 0.5, 1.0 mm and the diameter (ø10 mm) on the flat plate. As two cameras size are 29 by 29 mm (camera model: Basler aca5472-17um and lens ML-U1217SR-18C), which allows the baseline B to be set as 50mm. The D is set to be 300 mm away from the target.

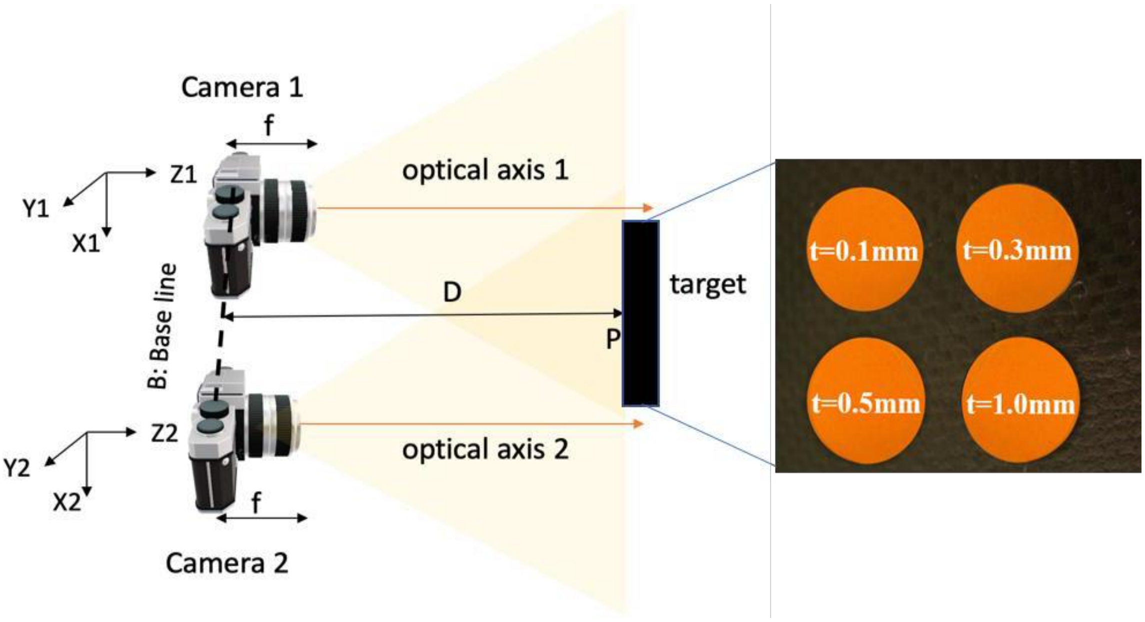

Figure 5.4. Experimental setup for stereoscopic 3D imaging.

Figure 5.5 shows the 3D reconstructed results surface map comparison, and figure 5.6 presents the horizontal linear scan results. The single reconstructed image was obtained by the stereoscopic methods on the distortion-removal images. The information of each pattern is related to the base structure, thus FSS method was applied to remove such effect. By identify the circular pattern's radius and center location, mask can be generated to separate the background and target information. The fitted background was generated by the bandpass filter combined with the low-pass filter and the high-pass filter was applied after the merging process. Each of the pattern information was extracted from the base structure. The FSS result is compared with the general bandpass filtered method, the gaussian-filtered method and reference measurement by the laser displacement sensor with 20 nm resolution.

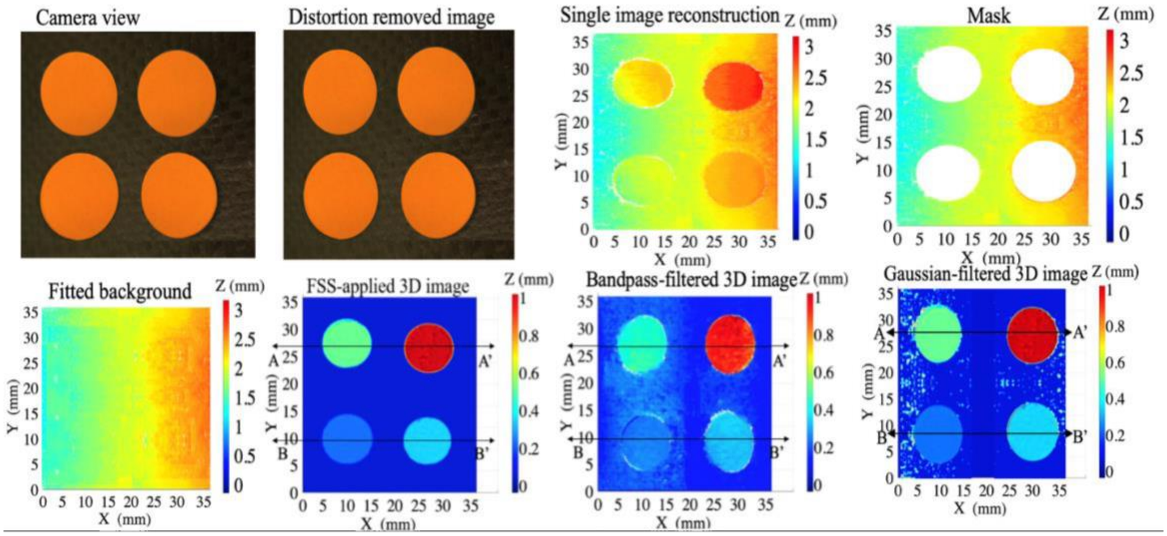

Figure 5.5. 3D imaging results: FSS, bandpass-filtered, gaussian-filtered 3D images.

Instead of separating the target information from the background, the conventional filtering method is based on the polynomial method to find the best fitted plan to the stereoscopic reconstructed map, then extract the pattern features. This method can present the target location and rough depth information, but the cross-talk effect between the pattern and base structure exists. The pattern profiles by the bandpass-filtered 3D imaging also showed a significant discrepancy with those of the laser displacement sensor. The Gaussian filter to the base structure was applied here for the comparison as well. This method can extract the pattern information well but the edge-effect, which is the noise information from the edge of image frame, exists, and we can observe this from the reconstructed map and the linear scan. Same high-pass filter was applied to remove the environmental noise for both methods.

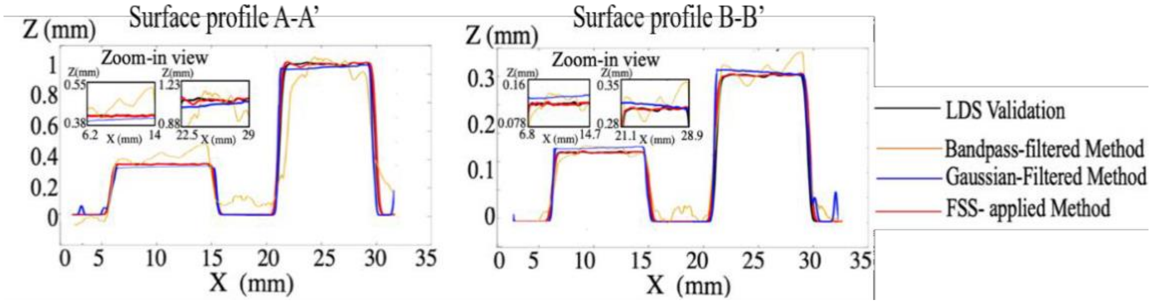

Figure 5.6. 3D imaging horizontal linear scan results: FSS, bandpass-filtered, gaussian-filtered 3D images.

This result shows that the filtering process applied to all features, including the patterns and background, involves the data, and bandpass filtering of the images involves data loss and lowers the spatial resolution of the image. The surface profiles of the FSS-applied 3D imaging method showed good agreement with the laser displacement sensor output, and the discrepancy was estimated at less than 1%. This result indicates that the 3D reconstructed image was spatially resolved by automatically recognizing and segmenting the features on the 2D images, locally and adaptively applying super-resolution algorithm to the segmented images based on the classified features, and then merging those filtered segments. As a result, the FSS and merging method is confirmed to significantly enhance the spatial resolution of the 3D stereoscopic images while preserving imaging features.

5.3.2. Strobo-Stereoscopy based ISE method

Guo combined stroboscopy and stereoscopy, enabling in-process 3D imaging while the measurement target is rotating [94], and recently introduced fluorescence strobo-stereoscopy to suppress specular reflection off the optical quality rod and patterned roll [116]. In this study, the FSS and merging method and strobo-stereoscopy algorithm were combined to in-process obtain spatially resolved 3D images of the rotating target, as seen in Figure 5.7.

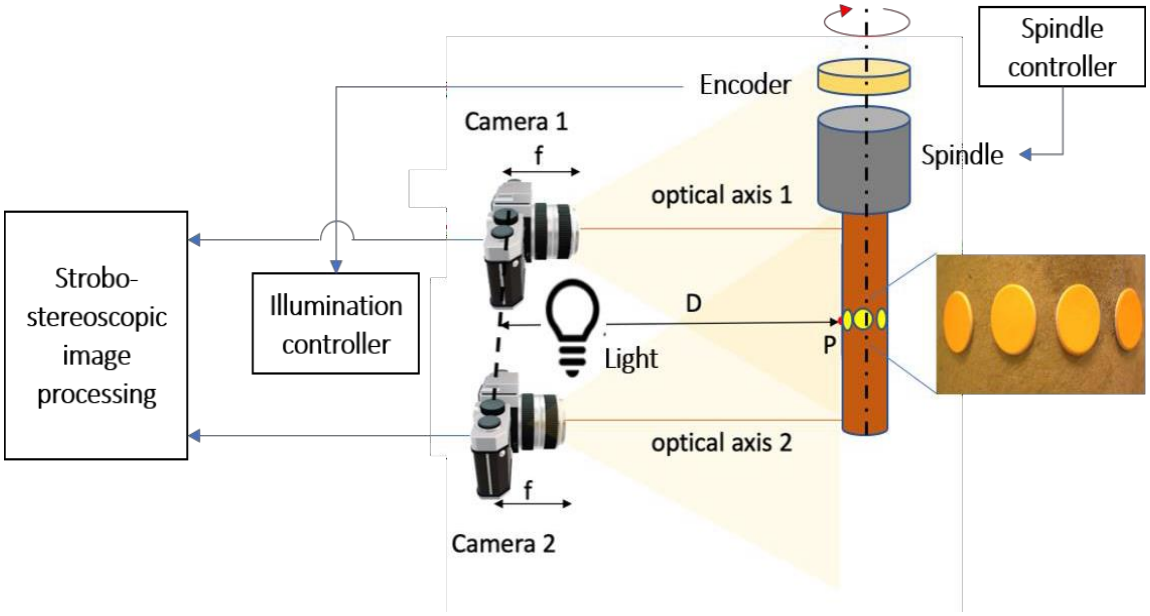

Figure 5.7. Experimental setup for strobo-stereoscopic 3D imaging.

While the stereoscopy algorithm can provide a 3D image at a specific measurement position, the phase-shifting of the strobo-light allows the whole-view reconstruction of the rotating target while the target is rotating with a frequency. The quadrature encoder outputs are feedback for the stroboscopic light on/off control, so the specific area of the measurement target can be illuminated by blinking the light-emitting diode (LED) light.

The 3D images were obtained at every 20-degree interval. The illumination system and camera system can be synchronized with the spindle motion. The 18 3D images reconstructed around the rod were systematically stitched to generate the full view image.

The stereoscopic image processing algorithm is typically for single image reconstruction. The phase unwrapping is required for the curve surface stitching process. In order to stitch the neighboring images conveniently and efficiently, FSS method were applied to the raw reconstructed surface map, thus the curve information from the base structure can be removed only the target information remained. The panorama full view map was reconstructed through the neighboring images stitching by defining the location of the overlapped patterns. Finally, 3D full-view stereoscopic images were obtained. The whole measurement and imaging processing operations were automated in the LABVIEW and MATLAB software environment, and the whole process took less than 1 second. In the experiment, the patterns were simply made by attaching the metal stickers (ø10 mm and 1 mm thickness). Those were randomly attached around the rod, and the rod was attached to the aerostatic spindle.

The FSS-applied strobo-stereoscopic 3D image was in-process obtained while the rod was rotating at a 100 revolution per minute (RPM). The reconstructed panorama full view image and the profile results showed that the pattern diameter, height, and interval were identified, as seen in Figure 5.8.

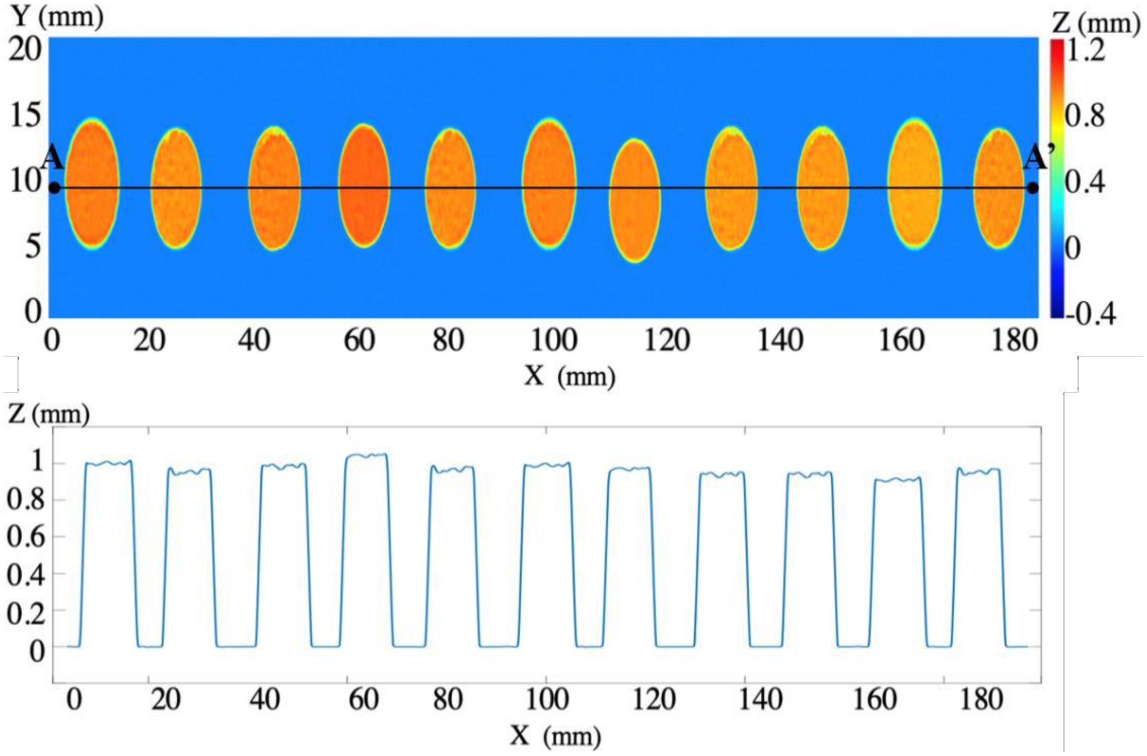

Figure 5.8. FSS-applied strobo-stereoscopic 3D image: full-view image (top) and A-A' profile (bottom).

The isometric view and top view of the rod with the 1.0 mm thick patterns were successfully reconstructed as seen in Figure 5.9.

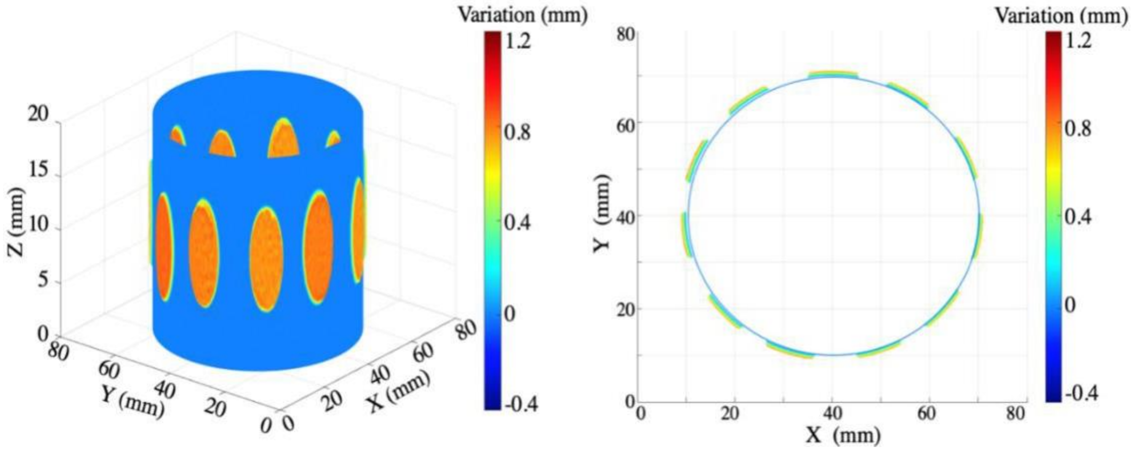

Figure 5.9. 3D strobo-stereoscopic image reconstruction results: isometric view (left) and top view (right).

In the same way, the metal stickers (ø10 mm and 0.1 mm thickness) were attached to the rod, and measured the 3D images as seen in Figures 5.10 and 5.11. Those results showed the potential of the FSS and merging method applicable to microscopy applications.

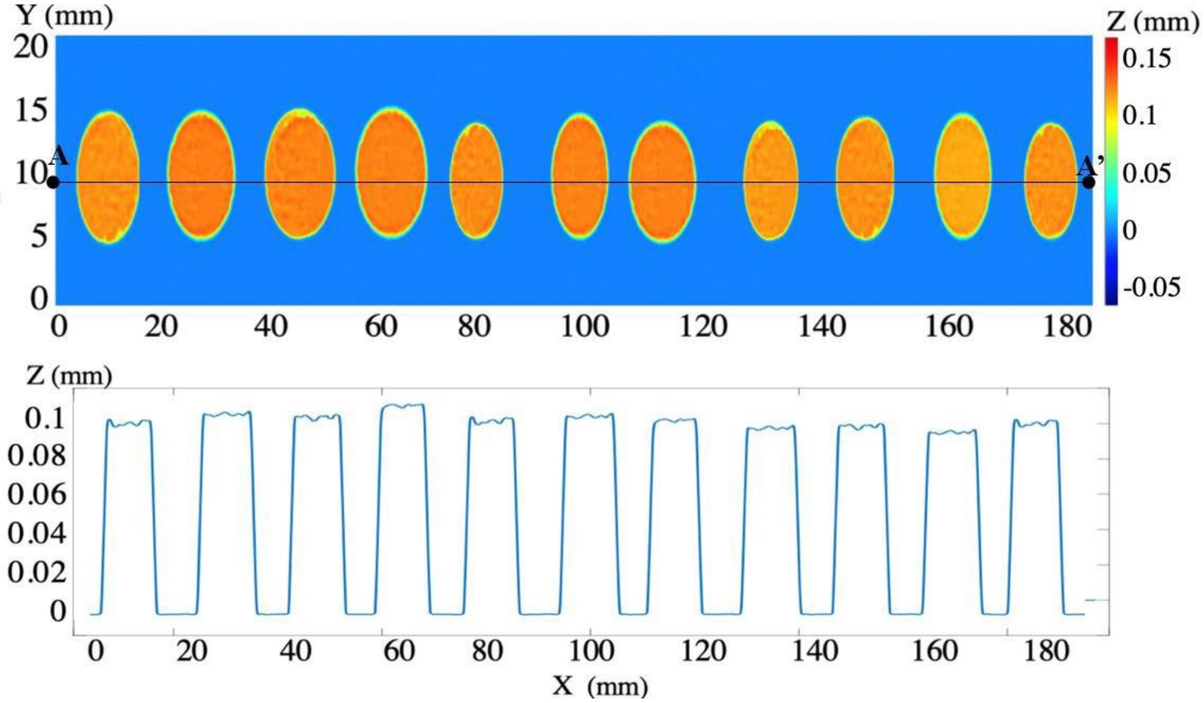

Figure 5.10. FSS-applied strobo-stereoscopic 3D image: full-view image (top) and A-A' profile (bottom).

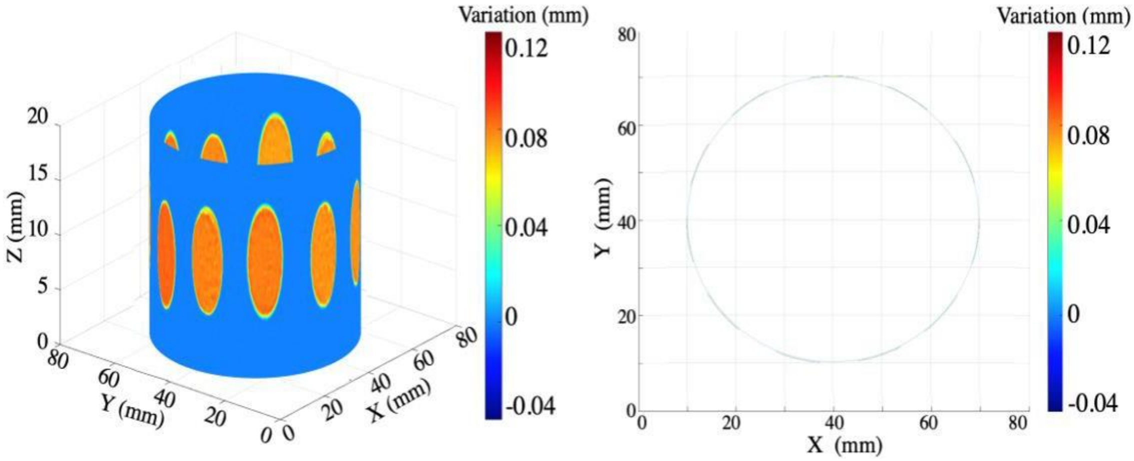

Figure 5.11. 3D strobo-stereoscopic image reconstruction results: isometric view (left) and top view (right).

5.4. Conclusion

The ISE and merging algorithm were implemented in the 3D imaging process for conventional stereoscopy and strobo-stereoscopy. The ISE image processing method was experimentally validated by reconstructing 3D stereoscopic images of the stationary and rotating targets. The image processing algorithm and convenient image stitching algorithm were developed to selectively separate the features from the background image and create a full-view image. The whole measurement and imaging processing were automated.

The experimental results showed that the ISE-processed 3D imaging method provides spatially resolved images compared with the conventional image filtering processes. The proposed 3D imaging method has a high potential to be adapted in various industrial applications requiring 3D visions. The feature extraction algorithms for various pattern shapes will be developed for future work, and those analysis methods for surface metrology and inspection will be studied. Also, the high-speed camera systems will be included to extend the measurement capability available for high-speed 3D imaging.

6. SUMMARY

6.1. Conclusion

This integral in-process surface 3D imaging technique is proposed with three systems based on the fundamental strobo-stereoscopy method. The entire 3D structure is rebuilt, and the surface quality and shape are monitored and inspected.

This dissertation provides a thorough analysis of three proposed systems, which are Strobo-Stereoscopy (SS), Fluorescent Strobo-Stereoscopy (FSS) and the Image Segmentation and Extraction (ISE). Figure 6.1 summarize the connection between the discussed techniques and principles through the dissertation.

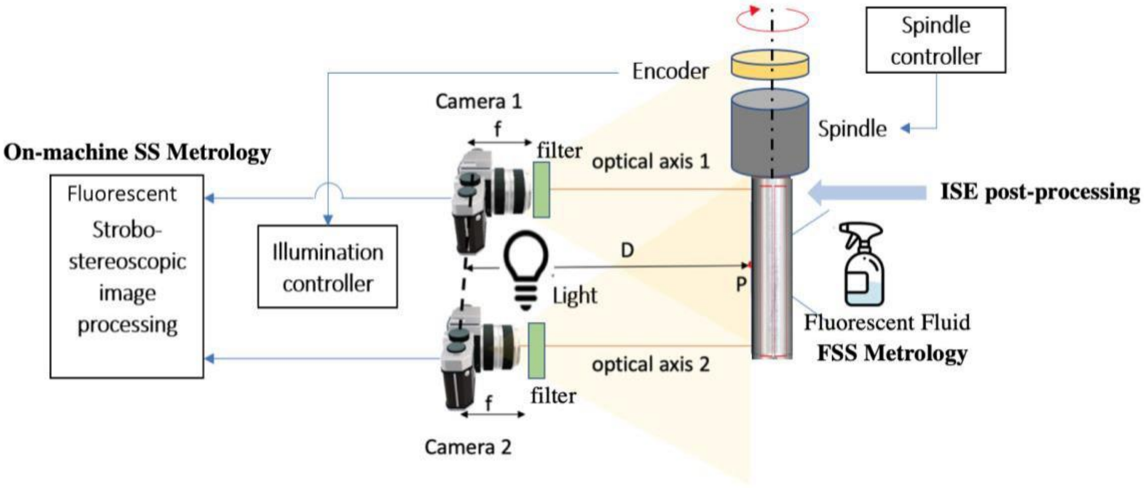

Figure 6.1. Summary of the proposed machine vision techniques in this dissertation.

Primary validation experiments on the cylinder shaft and patterned roll was conducted. Fluorescent fluid is used to characterize defects and to increase the capability of the primary Strobo-Stereoscopy setup for monitoring high reflective, non-distinct patterned surface. The full-reversal method can be used to determine certain GD&T

characteristics, such as circularity and cylindricity. The program for automated the strobo-stereoscopy monitoring process was developed. Proposed image segmentation and extraction post-processing techniques based on the filtering process is employed for target structure recognition and inspection from 3D surface map free from the freeform base structure.

These direct vision view results for targets in-motion inspection along with the easy constructed hardware structure will benefit the field of on-machine metrology manufacturing system and helped with the automation quality control.

6.2. Limitation and Future work

Two main limitations exist on the proposed system. One is the target surface depth/ slope-variation, another is the measurement accuracy.

The depth variation exist on the target sample should be within the depth of field allowance in the camera system. This is decided by the lens choices. Targets which are out of focus range and are blur in the camera view will cause false read out. The change of slope of the surface should be continuous. As the sudden change of the slope will cause discontinuous value on the contrast, which fundamentally comes from the change of the reflection light's direction. From the discussed illumination limitation, surfaces with sharp edges are not suitable for the stereoscopy technique. Moreover, fluorescent fluid is difficult to applied on such surface structure, as the applied fluid layer is required to be thin and consistent.

Thus, for the FSS system implement, detailed surface expansion characteristics for the fluorescent fluid will be studied to generate evenly distributed thin layer across the surface regardless of the slope variation. Moreover, multi-channel FSS will be proposed by applying the mixed fluorescent compounds which will generate multiple shifted emission wavelength. Along with mechanically shifted long pass filter, surface response in different wavelength range will be analyzed, reconstructed surface accuracy will be compared with the single channel FSS method.

For the Existed Strobo-Stereoscopy system, Spectroscopy will be implemented with the RGB laser source, thus the spectroscopic response under different wavelength will be analyzed for micron pattern inspection. Figure 6.2 presents the methodology for the Strobo-Stereo-Spectroscopy (SSS) system.

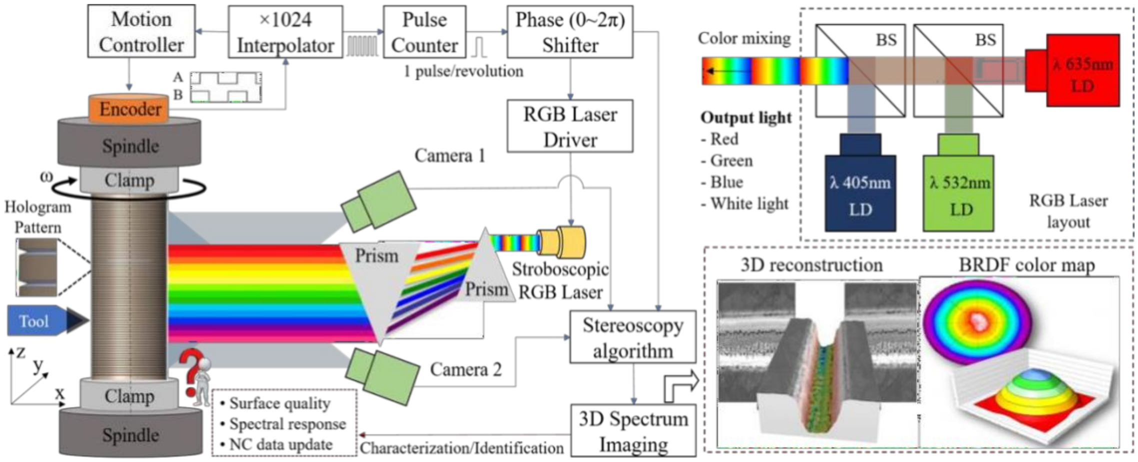

Figure 6.2. Strobo-Stereo-Spectroscopy technique methodology.

Measurement resolution is in the range of 1 to 100 microns based on the CCD resolution for the stereoscopy method. The resolution is fundamentally limited by the feature matching for the stereoscopic calibration process. When extract the feature from the natural surface, similar geometries or textures cause ambiguity to the calibration process.

In order to cope with scenes that lack features, a texture need to be forced by artificially projecting a particular pattern over the scene. Structure light is commonly involved with this study.

Here, correspondingly, dual-mode structure light based multichannel stereoscopy will be proposed as it is shown in figure 6.3. The projector with UV light source and LED light source will be employed to generate the structure light (sinusoidal fringe patterns). When the UV light is on, this could be applied with the fluorescent fluid applied surface. When the LED light is on, common rough surface will be examined.

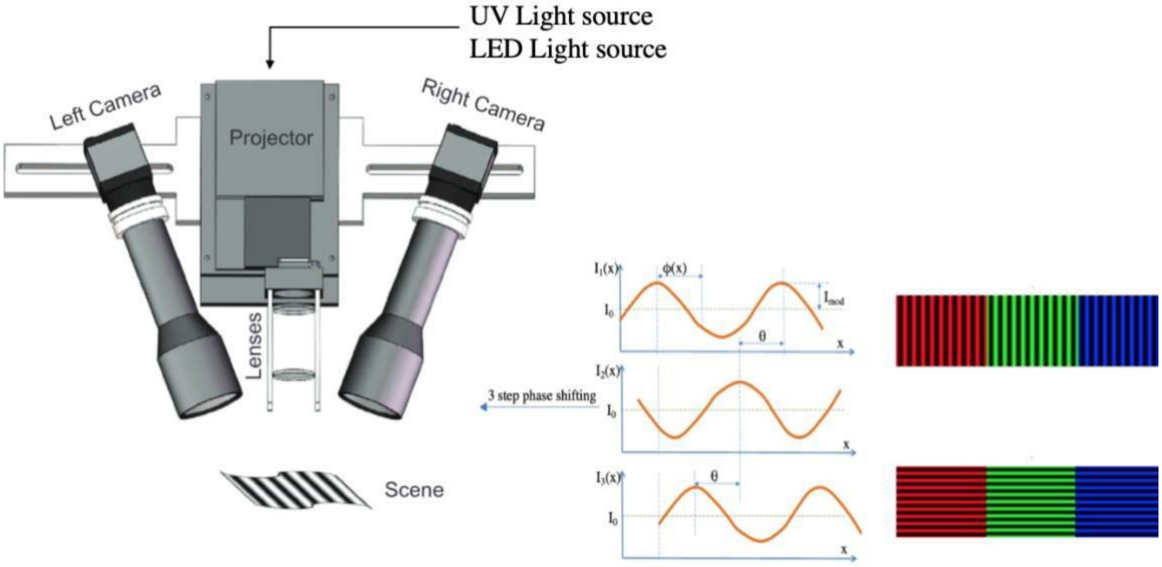

Figure 6.3. Dual mode structure light based multi-channel stereoscopy.

Triangulation is used to connect points on the projected pattern, projected pattern on the target surface and the patterns from the camera view. The 3D view can be reconstructed in a variety of different surface quality situations by varying the frequency of the sinusoidal pattern. In figure 6.3, $I_1(x,y)$, $I_2(x,y)$ and $I_3(x,y)$ are the intensities of three fringe patterns, $I_0(x,y)$ is the DC component (background), $I_{mod}(x,y)$ is the modulation signal amplitude, $\phi(x,y)$ is the phase, and θ is the constant phase-shift angle.

While the phase information is :

$$\varphi(x,y) = arctan\,[\sqrt{3}\frac{I_1(x,y)-I_3(x,y)}{2I_2(x,y)-I_1(x,y)-I_3(x,y)}] + 2k\pi \tag{14}$$

where k is an integer representing projection period, the depth:

$$Z = \frac{L}{B}(\varphi - \varphi_0) \tag{15}$$

where B is the distance between the projection to the camera, L is the depth between the reference plane to the camera, thus the depth variation on the surface can be calculated.

The current ISE method is applied for regular shaped surface, like circular or square shape. Further studies on the arbitrary edge targets will be included for testing. To remove the hardware installation uncertainty and fasten the testing speed, we will propose the single stereoscopic technique, the schematic is presented in figure 6.4.

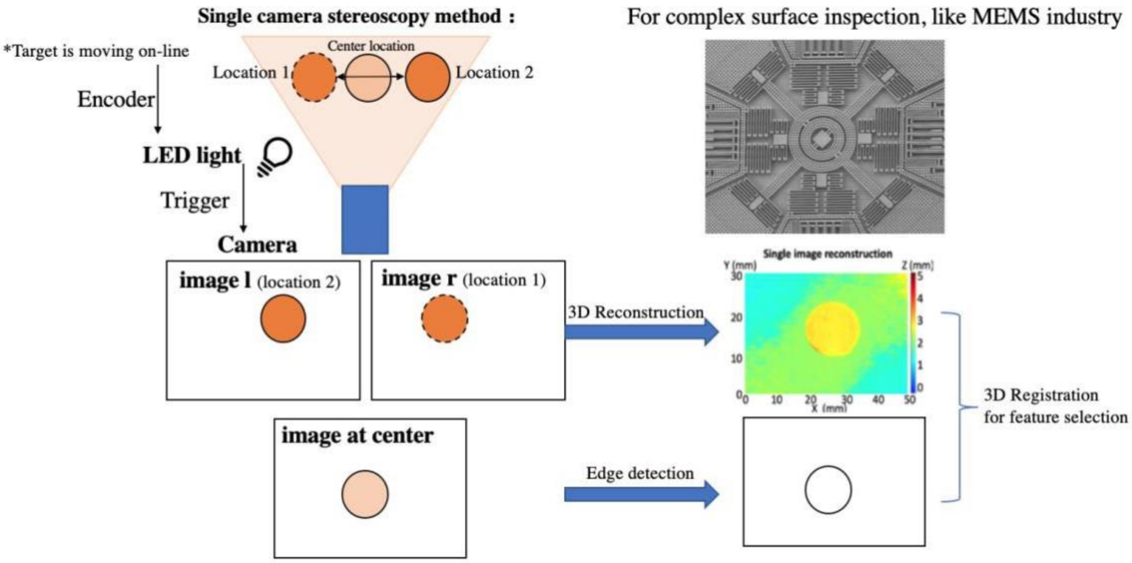

Figure 6.4. Adaptive single stereoscopic feature extraction system.

Instead of applying a pair of cameras, single camera is applied, by moving targets at left and right location, a virtual pair of cameras will be generated and calibrated, thus the 3D surface map can be reconstructed. A separate image when the target is faced normal to the camera will be captured for edge detection. By registering the 3D image and the edge detected map, arbitrary pattern can be extracted from the reconstructed surface map.

REFERENCES

1. Bai, C., Dallasega, P., Orzes, G., & Sarkis, J. (2020). Industry 4.0 technologies assessment: A sustainability perspective. International Journal of Production Economics, 229, 107776.
2. Colombo, A. W., Karnouskos, S., & Bangemann, T. (2014). Towards the next generation of industrial cyber-physical systems. In Industrial cloud-based cyber-physical systems (pp. 1–22). Springer.
3. Majstorovic, V. D., Durakbasa, N., Takaya, Y., & Stojadinovic, S. (2019). Advanced manufacturing metrology in context of industry 4.0 model. In International Conference on Measurement and Quality Control-Cyber Physical Issue (pp. 1–11). Springer.
4. Zhong, R. Y., Xu, X., Klotz, E., & Newman, S. T. (2017). Intelligent manufacturing in the context of industry 4.0: a review. Engineering, 3(5), 616–630.
5. Lee, J., Bagheri, B., & Kao, H.-A. (2015). A cyber-physical systems architecture for industry 4.0-based manufacturing systems. Manufacturing Letters, 3, 18–23.
6. Zezulka, F., Marcon, P., Vesely, I., & Sajdl, O. (2016). Industry 4.0–An Introduction in the phenomenon. IFAC-PapersOnLine, 49(25), 8–12.
7. Imkamp, D., Berthold, J., Heizmann, M., Kniel, K., Manske, E., Peterek, M., … Sommer, K.-D. (2016). Challenges and trends in manufacturing measurement technology–the “Industrie 4.0” concept. Journal of Sensors and Sensor Systems, 5(2), 325–335.

8. Täuscher, K. (2016). Business Models in the Digital Economy: An Empirical Study of Digital Marketplaces. Fraunhofer Center for International Management and Knowledge Economy, Leipzig.
9. Milošević, M., Đurđev, M., Lukić, D., Antić, A., & Ungureanu, N. (2020). Intelligent process planning for smart factory and smart manufacturing. In Proceedings of 5th International Conference on the Industry 4.0 Model for Advanced Manufacturing (pp. 205–214). Springer.
10. Berthold, J., & Imkamp, D. (2013). Looking at the future of manufacturing metrology: roadmap document of the German VDI/VDE Society for Measurement and Automatic Control. Journal of Sensors and Sensor Systems, 2(1), 1–7.
11. Lazzari, A., Pou, J.-M., Dubois, C., & Leblond, L. (2017). Smart metrology: the importance of metrology of decisions in the big data era. IEEE Instrumentation & Measurement Magazine, 20(6), 22–29.
12. Filz, M., Gellrich, S., Turetskyy, A., Wessel, J., Herrmann, C., & Thiede, S. (2020). Virtual Quality Gates in Manufacturing Systems: Framework, Implementation and Potential. Implementation and Potential. Journal of Manufacturing and Materials Processing, 4(4), 106.
13. Sousa, M. C., & Almeida, M. F. L. (2021). Smart revolution and metrology: A longitudinal science mapping approach. Measurement: Sensors, 18, 100340.
14. Ferrantino, M. J., & Koten, E. E. (2019). Understanding Supply Chain 4.0 and its potential impact on global value chains. Global Value Chain Development Report 2019, 103.

15. Marmolejo-Saucedo, J., & Hartmann, S. (2020). Trends in digitization of the supply chain: A brief literature review. EAI Endorsed Transactions on Energy Web, 7(29).

16. Serrano-Ruiz, J. C., Mula, J., & Poler, R. (2021). Smart Master Production Schedule for the Supply Chain: A Conceptual Framework. Computers, 10(12), 156.

17. Alonso, V., Dacal-Nieto, A., Barreto, L., Amaral, A., & Rivero, E. (2019). Industry 4.0 implications in machine vision metrology: an overview. Procedia Manufacturing, 41, 359–366.

18. Pfeifer, T., & Schmitt, R. (2011). Fertigungsmesstechnik. Oldenbourg Wissenschaftsverlag.

19. Schmitt, R. H., & Voigtmann, C. (2017). Sensorinformationen als Dienst–Baustein der vernetzten Produktion. Tm-Technisches Messen, 84(5), 296–309.

20. Mourtzis, D., Doukas, M., Psarommatis, F. (2015). A toolbox for the design, planning and operation of manufacturing networks in a mass customisation environment, Journal of Manufacturing Systems, 36, 2015, 274-286.

21. Mourtzis, D., Gargallis, A., Angelopoulos, J., & Panopoulos, N. (2020). An Adaptive Scheduling Method Based on Cloud Technology: A Structural Steelwork Industry Case Study. In Proceedings of 5th International Conference on the Industry 4.0 Model for Advanced Manufacturing (pp. 1–14). Springer.

22. Song, J.-F., & Vorburger, T. V. (1991). Stylus profiling at high resolution and low force. Applied Optics, 30(1), 42–50.

23. Binnig, G., Quate, C. F., & Gerber, C. (1986). Atomic force microscope. Physical Review Letters, 56(9), 930.

24. Minsky, M. (1961). Microscopy apparatus US patent 3013467. USP Office, Ed. US.

25. Minsky, M. (1988). Memoir on inventing the confocal scanning microscope. Scanning, 10(4), 128–138.

26. Conroy, M., & Armstrong, J. (2005). A comparison of surface metrology techniques. In Journal of Physics: Conference Series (Vol. 13, p. 106). IOP Publishing.

27. Hamilton, D. K., & Wilson, T. (1982). Surface profile measurement using the confocal microscope. Journal of Applied Physics, 53(7), 5320–5322.

28. Tiziani, H. J., & Uhde, H.-M. (1994). Three-dimensional image sensing by chromatic confocal microscopy. Applied Optics, 33(10), 1838–1843.

29. Hariharan, P. (1991). Optical interferometry. Reports on Progress in Physics, 54(3), 339.

30. Mathia, T. G., Pawlus, P., & Wieczorowski, M. (2011). Recent trends in surface metrology. Wear, 271(3–4), 494–508.

31. Fercher, A. F. (1976). Computer-generated holograms for testing optical elements: error analysis and error compensation. Optica Acta: International Journal of Optics, 23(5), 347–365.

32. Cai, W., Zhou, P., Zhao, C., & Burge, J. H. (2013). Analysis of wavefront errors introduced by encoding computer-generated holograms. Applied Optics, 52(34), 8324–8331.

33. Golnabi, H., & Asadpour, A. (2007). Design and application of industrial machine vision systems. Robotics and Computer-Integrated Manufacturing, 23(6), 630–637.

34. Oni, A. O. (2007). Development of a machine vision system for measurement of tool wear and surface roughness. Unpublished M. Sc. Dissertation, University of Ibadan, Nigeria.

35. Hoy, D. E. P., & Yu, F. (1991). Surface quality assessment using computer vision methods. Journal of Materials Processing Technology, 28(1–2), 265–274.

36. Ashour, M. W., Khalid, F., Halin, A. A., & Abdullah, L. N. (2015). Machining process classification using PCA reduced histogram features and the Support Vector Machine. In 2015 IEEE International Conference on Signal and Image Processing Applications (ICSIPA) (pp. 414–418). IEEE.

37. Charan, A., Chowdary, C. K., & Komal, P. (2022). The Future of Machine Vision in Industries- A systematic review. {IOP} Conference Series: Materials Science and Engineering, 1224(1), 12027. https://doi.org/10.1088/1757-899x/1224/1/012027

38. Krishna, A. V., Flys, O., Reddy, V. V, & Rosén, B. G. (2018). Surface topography characterization using 3D stereoscopic reconstruction of SEM images. Surface Topography: Metrology and Properties, 6(2), 24006.

39. Zhongxiang, H., Lei, Z., Jiaxu, T., Xuehong, M., & Xiaojun, S. (2009). Evaluation of three-dimensional surface roughness parameters based on digital image processing. The International Journal of Advanced Manufacturing Technology, 40(3), 342–348.

40. Niu, M., Song, K., Huang, L., Wang, Q., Yan, Y., & Meng, Q. (2020). Unsupervised saliency detection of rail surface defects using stereoscopic images. IEEE Transactions on Industrial Informatics, 17(3), 2271–2281.

41. Sarker, M., Dias-da-Costa, D., & Hadigheh, S. A. (2019). Multi-scale 3D roughness quantification of concrete interfaces and pavement surfaces with a single-camera set-up. Construction and Building Materials, 222, 511–521.

42. Lee, H., Kim, M. Y., & Moon, J. Il. (2017). Three-dimensional sensing methodology combining stereo vision and phase-measuring profilometry based on dynamic programming. Optical Engineering, 56(12), 124107.

43. Yang, L., Li, E., Long, T., Fan, J., Mao, Y., Fang, Z., & Liang, Z. (2018). A welding quality detection method for arc welding robot based on 3D reconstruction with SFS algorithm. The International Journal of Advanced Manufacturing Technology, 94(1), 1209–1220.

44. Bračun, D., & Sluga, A. (2015). Stereo vision based measuring system for online welding path inspection. Journal of Materials Processing Technology, 223, 328–336.

45. Gao, W., Haitjema, H., Fang, F. Z., Leach, R. K., Cheung, C. F., Savio, E., & Linares, J.-M. (2019). On-machine and in-process surface metrology for precision manufacturing. CIRP Annals, 68(2), 843–866.

46. Quinsat, Y., & Tournier, C. (2012). In situ non-contact measurements of surface roughness. Precision Engineering, 36(1), 97–103.

47. Wade, N. J. (2002). Charles Wheatstone (1802–1875). Perception. SAGE Publications Sage UK: London, England.

48. Greenslade Jr, T. B. (1972). The first stereoscopic pictures of the Moon. American Journal of Physics, 40(4), 536–540.

49. Barnard, S. T., & Fischler, M. A. (1982). Computational stereo. ACM Computing Surveys (CSUR), 14(4), 553–572.

50. Cochran, S. D., & Medioni, G. (1992). 3-D surface description from binocular stereo. IEEE Transactions on Pattern Analysis & Machine Intelligence, 14(10), 981–994.

51. Guo, X., & Lee, C. (2021). Preliminary study of phase-shifting strobo-stereoscopy for cutting tool monitoring. Journal of Manufacturing Processes, 64, 1214–1222.

52. Luhmann, T. (2010). Close range photogrammetry for industrial applications. ISPRS Journal of Photogrammetry and Remote Sensing, 65(6), 558–569.

53. Brown, D. C. (1971). Close-range camera calibration, Photogrammetric Engineering. Engineering and Remote Sensing, 37(8), 855–866.

54. Weng, J., Cohen, P., & Herniou, M. (1992). Camera calibration with distortion models and accuracy evaluation. IEEE Transactions on Pattern Analysis and Machine Intelligence, 14(10), 965–980.

55. Wang, J., Shi, F., Zhang, J., & Liu, Y. (2008). A new calibration model of camera lens distortion. Pattern Recognition, 41(2), 607–615.

56. Zhang, Z., Deriche, R., Faugeras, O., & Luong, Q.-T. (1995). A robust technique for matching two uncalibrated images through the recovery of the unknown epipolar geometry. Artificial Intelligence, 78(1–2), 87–119.

57. Huang, R.(2015), "High precision optical surface metrology using deflectometry", Ph.D., University of Arizona

58. Ozanian, T. (1995). Approaches for stereo matching.

59. Faugeras, O., Hotz, B., Mathieu, H., Viéville, T., Zhang, Z., Fua, P.,…,Vuillemin, J. (1993). Real time correlation-based stereo: algorithm, implementations and applications. Inria.

60. Liu, S., Zhao, L., & Li, J. (2012). The applications and summary of three dimensional reconstruction based on stereo vision. In 2012 International Conference on Industrial Control and Electronics Engineering (pp. 620–623). IEEE.

61. Li, D., & Tian, J. (2013). An accurate calibration method for a camera with telecentric lenses. Optics and Lasers in Engineering, 51(5), 538–541.

62. Schreier, H. W., Garcia, D., & Sutton, M. A. (2004). Advances in light microscope stereo vision. Experimental Mechanics, 44(3), 278–288.

63. Marinello, F., Bariani, P., Savio, E., Horsewell, A., & De Chiffre, L. (2008). Critical factors in SEM 3D stereo microscopy. Measurement Science and Technology, 19(6), 65705.

64. Jin, P., Liu, J. H., Liu, S. L., & Wang, X. (2016). Automatic multi-stereo-vision reconstruction method of complicated tubes for industrial assembly. Assembly Automation.

65. Zhang, Q. (2005). Optical 3-D shape and deformation measurement of rotating blades using stroboscopic structured illumination. Optical Engineering, 44(11), 113601. https://doi.org/10.1117/1.2127927

66. Kimura, Y., Naito, T., Nakano, M., Moribe, H., & Kuno, T. (1995). Stereo vision system for car assembly. In Proceedings of 1995 IEEE International Conference on Robotics and Automation (Vol. 2, pp. 1403–1409). IEEE.

67. Susemihl, H., Moeller, C., Kothe, S., Schmidt, H. C., Shah, N., Brillinger, C., … Hintze, W. (2016). High accuracy mobile robotic system for machining of large aircraft components. SAE International Journal of Aerospace, 9(2), 231.

68. Podrekar, G., Tomaževič, D., Likar, B., & Usenik, P. (2017). Model based visual inspection of pharmaceutical tablets with photometric stereo. In 2017 Fifteenth IAPR International Conference on Machine Vision Applications (MVA) (pp. 133–136). IEEE.

69. Moore, R. J. D., Thurrowgood, S., Bland, D., Soccol, D., & Srinivasan, M. V. (2009). A stereo vision system for uav guidance. In 2009 IEEE/RSJ International Conference on Intelligent Robots and Systems (pp. 3386–3391). IEEE.

70. Hussein, A., Marín-Plaza, P., Martín, D., de la Escalera, A., & Armingol, J. M. (2016). Autonomous off-road navigation using stereo-vision and laser-rangefinder fusion for

outdoor obstacles detection. In 2016 IEEE Intelligent Vehicles Symposium (IV) (pp. 104–109). IEEE.

71. Marrugo, A. G., Gao, F., & Zhang, S. (2020). State-of-the-art active optical techniques for three-dimensional surface metrology: a review. JOSA A, 37(9), B60–B77.

72. Chen, T., Lensch, H. P. A., Fuchs, C., & Seidel, H.-P. (2007). Polarization and phase-shifting for 3D scanning of translucent objects. In 2007 IEEE conference on computer vision and pattern recognition (pp. 1–8). IEEE.

73. Lin, H., Gao, J., Zhang, G., Chen, X., He, Y., & Liu, Y. (2017). Review and comparison of high-dynamic range three-dimensional shape measurement techniques. Journal of Sensors, 2017.

74. Liu, G., Liu, X.-Y., & Feng, Q.-Y. (2011). 3D shape measurement of objects with high dynamic range of surface reflectivity. Applied Optics, 50(23), 4557–4565.

75. Guo, X., Chen, Y., Wang, C., Cheng, M., Wen, C., & Yu, J. (2016). Automatic shape-based target extraction for close-range photogrammetry. In Int. Arch. Photogramm. Remote Sens. Spatial Inf. Sci. (Vol. 41, pp. 583–587).

76. Dong, B., Li, C., & Pan, B. (2020). Fluorescent digital image correlation applied for macroscale deformation measurement. Applied Physics Letters, 117(4), 44101.

77. Seo, Y. B., Jeong, H. Bin, Rhee, H.-G., Ghim, Y.-S., & Joo, K.-N. (2020). Single-shot freeform surface profiler. Optics Express, 28(3), 3401–3409.

78. Terzić, K., & Hansard, M. (2016). Methods for reducing visual discomfort in stereoscopic 3D: A review. Signal Processing: Image Communication, 47, 402–416.

79. Klinker, G. J., Shafer, S. A., & Kanade, T. (1988). The measurement of highlights in color images. International Journal of Computer Vision, 2(1), 7–32.

80. Wolff, L. B., & Boult, T. E. (1993). Constraining object features using a polarization reflectance model. Phys. Based Vis. Princ. Pract. Radiom, 1, 167.

81. Gao, Z., Hwang, A., Zhai, G., & Peli, E. (2018). Correcting geometric distortions in stereoscopic 3D imaging. PloS One, 13(10), e0205032.

82. Martin, D. (2007). A practical guide to machine vision lighting. Midwest Sales and Support Manager, Adv Illum2007, 1–3.

83. Gorevoy, A. V, Machikhin, A. S., Khokhlov, D. D., & Batshev, V. I. (2020). Optimization of prism-based stereoscopic imaging systems at the optical design stage with respect to required 3D measurement accuracy. Optics Express, 28(17), 24418–24430.

84. Shin, D., & Javidi, B. (2012). Three-dimensional imaging and visualization of partially occluded objects using axially distributed stereo image sensing. Optics Letters, 37(9), 1394–1396.

85. Abookasis, D., & Rosen, J. (2006). Stereoscopic imaging through scattering media. Optics Letters, 31(6), 724–726.

86. Hu, Z., Luo, H., Du, Y., & Lu, H. (2013). Fluorescent stereo microscopy for 3D surface profilometry and deformation mapping. Optics Express, 21(10), 11808–11818.

87. Berfield, T. A., Patel, J. K., Shimmin, R. G., Braun, P. V, Lambros, J., & Sottos, N. R. (2006). Fluorescent image correlation for nanoscale deformation measurements. Small, 2(5), 631–635.

88. Hu, Z., Xu, T., Luo, H., Gan, R. Z., & Lu, H. (2016). Measurement of thickness and profile of a transparent material using fluorescent stereo microscopy. Optics Express, 24(26), 29822–29829.

89. Samuel, B. A., Demirel, M. C., & Haque, A. (2007). High resolution deformation and damage detection using fluorescent dyes. Journal of Micromechanics and Microengineering, 17(11), 2324.

90. Surface Texture (Roughness, Waviness, Lay) (2020). ASME B46.1-2019.

91. Mira, M. (n.d.). Extrapolating Lessons for Future Cinematic Virtual Reality Creators by Looking at Current and Past Attempts at Creating Virtual Reality.

92. Hariharan, P. (2010). Basics of interferometry. Elsevier.

93. Zhang, Y., Gibson, G. M., Hay, R., Bowman, R. W., Padgett, M. J., & Edgar, M. P. (2015). A fast 3D reconstruction system with a low-cost camera accessory. Scientific Reports, 5(1), 1–7.

94. Sheppard, C. J. R., & Hamilton, D. K. (1983). High resolution stereoscopic imaging. Applied Optics, 22(6), 886–887.

95. Kassamakov, I., Lecler, S., Nolvi, A., Leong-Hoï, A., Montgomery, P., & Hæggström, E. (2017). 3D super-resolution optical profiling using microsphere enhanced Mirau interferometry. Scientific Reports, 7(1), 1–7.

96. Song, W., Choi, S., Jeong, S., & Sohn, K. (2020). Stereoscopic image super-resolution with stereo consistent feature. In Proceedings of the AAAI Conference on Artificial Intelligence (Vol. 34, pp. 12031–12038).

97. Yan, T., Jiao, J., Liu, W., & Lau, R. W. H. (2019). Stereoscopic image generation from light field with disparity scaling and super-resolution. IEEE Transactions on Image Processing, 29, 1827–1842.

98. Carles, G., Downing, J., & Harvey, A. R. (2014), Super-resolution imaging using a camera array, Optical Letter, 39 (7), 1889-1892.

99. Eun, D., Jang, R., Ha, W. S., Lee, H., Jung, S. C., & Kim, N. (2020). Deep-learning-based image quality enhancement of compressed sensing magnetic resonance imaging of vessel wall: Comparison of self-supervised and unsupervised approaches. Scientific Reports, 10(1), 1–17.

100. Khan, R., Yang, Y., Liu, Q., Shen, J., & Li, B. (2021). Deep image enhancement for ill light imaging. JOSA A, 38(6), 827–839.

101. Yoo, S. B., & Lee, E.-J. (2020). Deep Super-Resolution Imaging Technology: Toward Optical Super-Vision. IEEE Consumer Electronics Magazine, 10(1), 24–31.

102. Sahin, E., Katkovnik, V., & Gotchev, A. (2016). Super-resolution in a defocused plenoptic camera: a wave-optics-based approach. Optics Letters, 41(5), 998–1001.

103. Zeng, Z., Xie, H., Chen, L., Zhanghao, K., Zhao, K., Yang, X., & Xi, P. (2017). Computational methods in super-resolution microscopy. Frontiers of Information Technology & Electronic Engineering, 18(9), 1222–1235.

104. Dong, C., Loy, C. C., He, K., & Tang, X. (2014). Learning a deep convolutional network for image super-resolution. In European conference on computer vision (pp. 184–199). Springer.

105. Farsiu, S., Robinson, D., Elad, M., & Milanfar, P. (2004). Advances and challenges in super-resolution. International Journal of Imaging Systems and Technology, 14(2), 47–57.

106. Ghanavati, S. (2017). Quantitative Analysis and Comparison of Cerebrovasculature in Common Mouse Strains: C57BL/6, CD-1, CBA, and 129/Sv using Imaging, Automatic Segmentation and Labelling of the Cerebral Vessels. University of Toronto (Canada).

107. Schubert, V. (2017). Super-resolution microscopy–applications in plant cell research. Frontiers in Plant Science, 8, 531.

108. Suri, J. S., Singh, S., & Reden, L. (2002). Computer vision and pattern recognition techniques for 2-D and 3-D MR cerebral cortical segmentation (Part I): a state-of-the-art review. Pattern Analysis & Applications, 5(1), 46–76.

109. Remeseiro, B., & Bolon-Canedo, V. (2019). A review of feature selection methods in medical applications. Computers in Biology and Medicine, 112, 103375.

110. Shao, F., Li, K., Lin, W., Jiang, G., & Yu, M. (2015). Using binocular feature combination for blind quality assessment of stereoscopic images. IEEE Signal Processing Letters, 22(10), 1548–1551.

111. Simonetto, E., Oriot, H., & Garello, R. (2005). Rectangular building extraction from stereoscopic airborne radar images. IEEE Transactions on Geoscience and Remote Sensing, 43(10), 2386–2395.

112. Stout, K. J., & Blunt, L. (2000). Three dimensional surface topography. Elsevier.

113. Raja, J., Muralikrishnan, B., & Fu, S. (2002). Recent advances in separation of roughness, waviness and form. Precision Engineering, 26(2), 222–235.

114. Sullivan, P. J. (2001). Surface topography filtering. In Metrology and properties of engineering surfaces (pp. 113–167). Springer.

115. Faugeras, O., & Faugeras, O. A. (1993). Three-dimensional computer vision: a geometric viewpoint. MIT press.

116. Guo, X., & Lee, C.B.(2022). Fluorescence strobo-stereoscopy for specular reflection-suppressed full field of view imaging. Measurement, 192, 110907.

APPENDIX A

CV

Xiangyu Guo

J. Mike Walker ’66 Department of Mechanical Engineering, Texas A&M University
JCAIN 441, College Station, TX, 77843-3123, USA
Email xiangyug33@tamu.edu Phone +1-520-331-3290

Education:

- BS. Opto-Electronics 2015, Xi’an Technological University (China).
- MS. Optical Sciences 2018, University of Arizona (Tucson, AZ).
- Ph.D. Mechanical Engineering, Texas A & M University (College Station, TX).

Area of Research:

- On-machine dimensional metrology (interferometry, microscopy, stereoscopy.).
- On-machine fabrication monitoring (strobe-stereoscopy, capacitive sensor monitoring.).
- Optical metrology (interferometry stereoscopy for mechanical fabrication system monitoring; Contact, interferometry or deflectometry methods for optical surfaces characteristics testing.).
- Optical Fabrication (CNC solution towards aspheric or freeform optics manufacture.).
- Surface Smoothing Process Control (grinding, polishing and smoothing process development and optimization for additive manufacturing material, ceramic, metal and glass, roughness parameters relationship.).
- Opto-Mechanical design (fabrication mold, assembling structure, etc.).

Research Experience:

Research Assistant, Texas A & M University, College Station, TX. 2019 ~ present

Surface Analyst, Optical Engineering and Fabrication Facility, 2018

Tucson, AZ. 2016 ~ 2018

Research Assistant, University of Arizona, Tucson, AZ.

Student Assistant, Xi'an Technological University, China 2014 ~ 2015

Research Projects:

On-Machine Metrology Development (2019-present).

- Honeywell Federal manufacturing & Technologies, LLC: Precision machining of AM components.
- Strobo-Stereoscopy on-machine machine tool metrology development.
- Fluorescent strobo-stereoscopy metrology development.
- Active strobo-stereoscopy metrology development.
- Roll-to-roll pattern recognition and quality analysis.
- Cosine error free surface and thickness profilometer development

Manufacturing Process (2016~2018).

- Chemical mechanical polishing (CMP) on SPDT Al 6061 Mirror.
- Zero CTE ceramic material Cordierite manufacturing process development.
- SiC based ZrB2 flat ceramic mirror manufacturing process development.

Surface Ultra-smoothing project (2016~2018).

- Clear photopolymer 3D-printed flat lens post-processing.
- Pseudo random unsophisticated CNC based freeform optics smoothing.
- Post-polishing on Hyperbolic 3D-Printed Lens.

Others (2015~2016).

- Post polishing on UHV window for laser vacuum chamber.
- Relationships between polishing methods and surface microscopic characterization**.**

Teaching:

- MEEN 260 Mechanical Measurements. 2020 Fall
- OPTI 415/515L Optical Specifications, Fabrication and Testing Lab. 2018 Spring
- OPTI 415 Optical Specifications, Fabrication and Testing. 2018 Spring
- OPTI 421/521 Introduction. to Optomechanical design. 2017 Fall

Journal Publications:

- **ChaBum Lee and Xiangyu Guo** , Spatially resolved stereoscopic surface profiling by using a feature-selective segmentation and merging technique**, Surf. Topogr.: Metrol. Prop. Vol.10, pp. 014002 (2022)**
- **Xiangyu Guo and ChaBum Lee, Fluorescence Strobo-Stereoscopy for Specular Reflection-Suppressed Full Field of View Imaging, Measurement, Vol. 192, pp. 110907 (2022)**
- **Xiangyu Guo** and **ChaBum Lee**, Preliminary study of phase-shifting strobo-stereoscopy for cutting tool monitoring, Journal of Manufacturing Processes, Vol. 64, pp. 1214-1222 (2021).
- **Xiangyu Guo** and **ChaBum Lee**, Cosine error-free metrology tool path planning for thickness profile measurements, ASME Journal of Manufacturing Science and Engineering, Vol. 143, 041006 (2021).
- Heebum Chun, **Xiangyu Guo**, Jungsub Kim, and ChaBum Lee, A review: additive manufacturing of flexure mechanism for nanopositioning system, The International Journal of Advanced Manufacturing Technology, Vol. 110, pp. 681-703 (2020)

- **Xiangyu Guo**, Jaemin Han, and ChaBum Lee, Cosine error elimination method for 1-dimensional convex and concave surface profile measurements, ASME, Journal of Manufacturing Science and Engineering, 142(4): 041001 (2020).
- **Xiangyu Guo**, Yong Shu, Geon-Hee Kim, Michael Palmer, Heejoo Choi, Dae Wook Kim, “Pseudo-random orbiting stroke for freeform optics post-processing”, Optical Engineering, Vol. 58, No. 9, pp. 92608 (2019).

Conference Publications:

- **Xiangyu Guo,** Cha Bum Lee, “Enhanced Three-Dimensional Surface Profiling Technique based on a Feature-Selective Segmentation and Merging”, MSEC Manufacturing Science and Engineering Conference, West Lafayette, IN. (2022).
- **Xiangyu Guo**, Jungsub Kim, Cha Bum Lee, “In-Process 3D Roll Pattern Measurement and Inspection by Strobo-Stereoscopy”, The Inaugural International Conference on Micro- and Nano-devices Enabled by R2R Manufacturing, Austin, TX.(2021).
- **Xiangyu Guo**, Jungsub Kim, Cha Bum Lee, “Preliminary study on Fluorescent Strobo-Stereoscopy”, Proceedings of 36th Annual Conference on American Society for Precision Engineering, Minneapolis, MN. (2021).
- Jay Raval, Aamer Kazi, **Xiangyu Guo**, ChaBum Lee, and Bruce Tai, Investigation of machinability of additively manufactured metal alloys, 2021 Annual International Solid Freeform Fabrication Symposium, Virtual Conference.(2021).
- **Xiangyu Guo**, Cha Bum Lee, “Phase- shifting 3D Imaging of Rotating Milling/Drilling tools”, Proceedings of 35th Annual Conference on American Society for Precision Engineering, Virtual Online. (2020).

- **Xiangyu Guo**, ChaBum Lee, " Non-contact, continuous, Synchronized, Cosine error-free thickness profile measurement by surface metrology tool path planning", ASME 15th Manufacturing Science and Engineering Conference, Cincinnati, OH. (2020) .
- **Xiangyu Guo**, Jaemin Han, Joshua A. Tarbutton, and ChaBum Lee, "Measurement Uncertainty Evaluation of Cosine Error-Free Surface Profile Measuring System", American Society for Precision Engineering, Pittsburgh, PA. (2019).
- Dae Wook Kim, Geon-Hee Kim, **Xiangyu Guo**, Logan Graves, Isaac Trumper, Yong Shu, Maham Aftab and Heejoo Choi, "Full Spectrum Big Data Analysis for Dynamic Freeform Optics Manufacturing", International Symposium on Precision Engineering and Sustainable Manufacturing (PRESM) (2019).
- Joseph Rice, Michael Hart, Erica Corral, **Xiangyu Guo**, and Dae Wook Kim, "Fabrication and Implementation of a New Ceramic Material in an Adaptive Optics System",Design and Fabrication Congress. (2017).
- Heejoo Choi, Isaac Trumper, **Xiangyu Guo**, Daniel Shannon, and Dae Wook Kim, "Extremely Large, Precise and Priceless Freeform Optics," International Conference on Positioning Technology. (2016).
- **Xiangyu Guo**, Ailing Tian, Yingge Zhang, "Relationships between Optical Polishing Methods and Parameters of Surface Microscopic characterization", China Western Conference of Photonics and Optical Engineering. (2015).

Activities:

- Academic Membership: ASPE, MSEC. 2019 ~ present
- Vice president: MEFEGs(Mechanical Engineering Female Grad Student, Texas A&M University) 2020 ~ present
- Member of WIO (Women in Optics, University of Arizona) 2016 ~ 2018

- Academic podcast host, editor: The Spotlight Report (available on iTunes) 2017 ~ 2019

Awards:

- 2021 James J. Cain Outstanding Graduate Student Award (from J. Mike Walker ’66 Department of Mechanical Engineering).
- 2020 ASPE Student Scholarship (from American Society of Precision Engineering).
- 2020 Walker Impact Award (from J. Mike Walker ’66 Department of Mechanical Engineering).
- 2020 MEEN Graduate Summer Research Grant (from J. Mike Walker ’66 Department of Mechanical Engineering).
- 2019 J. Mike Walker ’66 Department of Mechanical Engineering Graduate Student Travel Fellowship.
- 2019 Emil Buehler Aerodynamic Analog Fellowship (from J. Mike Walker ’66 Department of Mechanical Engineering).